Development and Application of the Model of Aerosol Dynamics, Reaction, Ionization and Dissolution (MADRID)

(first submission to JGR, Feb. 12, 2003
revised and submitted on June 5, 2003)

Yang Zhang, Betty Pun, Krish Vijayaraghavan, Shiang-Yuh Wu
and Christian Seigneur
Atmospheric and Environmental Research, Inc.
San Ramon, CA

Spyros N. Pandis
Department of Chemical Engineering, Carnegie-Mellon University
Pittsburgh, PA

Mark Z. Jacobson
Department of Civil and Environmental Engineering, Stanford University
Stanford, CA

Athanasios Nenes* and John H. Seinfeld
Department of Chemical Engineering and Division of Engineering and Applied Science,
California Institute of Technology
Pasadena, CA

* Current address: Schools of Earth and Atmospheric Sciences and Chemical Engineering, Georgia Institute of Technology

ABSTRACT

A new aerosol model, the Model of Aerosol Dynamics, Reaction, Ionization and Dissolution (MADRID) has been developed to simulate atmospheric particulate matter (PM). MADRID and the Carnegie-Mellon University (CMU) bulk aqueous-phase chemistry have been incorporated into the 3-D Models-3/Community Multiscale Air Quality model (CMAQ). The resulting model, CMAQ-MADRID, is applied to simulate the August 1987 episode in the Los Angeles basin. Model performance for ozone and PM is consistent with current performance standards. However, organic aerosol was underpredicted at most sites due to underestimation of primary organic PM emissions and secondary organic aerosol (SOA) formation. Nitrate concentrations were also sometimes underpredicted due mainly to overpredictions in vertical mixing, underpredictions in relative humidity and uncertainties in the emissions of primary pollutants. Including heterogeneous reactions changed hourly O_3 by up to 17% and 24-hr average $PM_{2.5}$, $sulfate_{2.5}$ and $nitrate_{2.5}$ concentrations by up to 3%, 7% and 19%, respectively. A SOA module with a mechanistic representation provides results that are more consistent with observations than that with an empirical representation. The moving-center scheme for particle growth predicts more accurate size distributions than a typical semi-Lagrangian scheme, which causes an upstream numerical diffusion. A hybrid approach that simulates dynamic mass transfer for coarse PM but assumes equilibrium for fine PM can predict a realistic particle size distribution under most conditions and the same applies under conditions with insignificant concentrations of reactive coarse particles to a bulk equilibrium approach that allocates transferred mass to different size sections based on condensational growth law. In contrast, a simple bulk equilibrium approach that allocates transferred mass based on a given distribution tends to cause a downstream numerical diffusion in the predicted particle size distribution.

1. INTRODUCTION

The demonstration of attainment of the National Ambient Air Quality Standards (NAAQS) (24-hour average and 3-year average concentrations) for particulate matter with aerodynamic diameter less than 2.5 μm ($PM_{2.5}$) and progress under the Regional Haze rule in the United States will require the use of three-dimensional (3-D) air quality models to evaluate the effect of various emission management options on $PM_{2.5}$ concentrations. These models will also be used in other areas due to the recent promulgation of a Canada-wide air quality standard for 24-hour average $PM_{2.5}$ concentrations and the forthcoming consideration of $PM_{2.5}$ standards by the European Union. Major episodic PM models include urban-scale models, mesoscale models and urban-through-global models. Examples of the urban-scale models include the Urban Airshed Model with Aerosols (UAM-AERO) [*Lurmann et al., 1997*], the California/Carnegie-Mellon Institute of Technology (CIT) model [*Meng et al.*, 1998] and the Urban Airshed Model with the Aerosol Inorganics Model (UAM-AIM) [*Sun and Wexler*, 1998a, 1998b]. Examples of the mesoscale models include the Regional Particulate Model (RPM) [e.g., *Binkowski and Shankar*, 1995], the Denver Air Quality Model- Versions 1 and 2 (DAQM and DAQM-V2) [*Middleton*, 1997; *RAQC*, 1999], the Models-3 Community Multiscale Air Quality (CMAQ) Modeling System [*Byun and Ching*, 1999] and the San Joaquin Valley Air Quality Study (SJVAQS) and the Atmospheric Utility Signatures Predictions and Experiments Study (AUSPEX) Regional Modeling Adaptation Project (SARMAP) Air Quality Model with Aerosols (SAQM-AERO) [*Pai et al.*, 2000]. An example of the urban-through-global models is GATOR [*Jacobson*, 1997a, 1997b]. These models have been applied to various airsheds including the Los Angeles Basin, CA (e.g., CIT, GATOR, SAQM-AERO, UAM-AERO, UAM-AIM and Models-3/CMAQ), Denver, CO (e.g., DAQM-V2) and the eastern North America (e.g., RPM and Models-3/CMAQ). Recent reviews of the

current status of 3-D air quality models for PM [*Seigneur et al.*, 1999; *Seigneur*, 2001; *Seigneur and Moran*, 2003] have suggested that existing 3-D models have several limitations in their treatment of aerosols that should be addressed before they can provide reliable results in a policy or regulatory context. For example, areas of improvements include the treatment of secondary PM formation (e.g. sulfate, nitrate and secondary organic aerosol (SOA)) and subgrid-scale plume treatment [*Seigneur et al.*, 1999]. In this work, we present the development of a new model for the treatment of PM processes and its incorporation into a 3-D host model, the U.S. Environmental Protection Agency (EPA) Models-3/CMAQ.

CMAQ is a 3-D grid-based air quality model that can be applied to simulate ozone (O_3) and other photochemical oxidants, PM, and the deposition of pollutants such as acidic and toxic air pollutants. CMAQ was selected as the 3-D host air quality model following a review of several existing 3-D models by *Seigneur et al.* [2000a]. Its original formulation has been described by *Byun and Ching* [1999]. The version used here is the August 2000 version released by EPA. The new modules incorporated into CMAQ include the Model of Aerosol Dynamics, Reaction, Ionization, and Dissolution (MADRID) and the Carnegie-Mellon University (CMU) bulk aqueous-phase chemical kinetic mechanism (hereafter referred to as the CMU bulk aqueous-phase chemical mechanism). In addition, some existing modules of CMAQ were modified either to be compatible with the new modules or to improve the representation of atmospheric processes. These new or modified modules are incorporated into CMAQ as options. The resulting model, CMAQ-MADRID, is applied to simulate the 27-28 August 1987 episode of the Southern California Air Quality Study (SCAQS) in the Los Angeles basin. Its performance is evaluated for O_3, $PM_{2.5}$, particulate matter with aerodynamic diameter less than 10 μm (PM_{10}) and PM chemical components, and compared with previous performance evaluations conducted with other PM models. Sensitivity studies are conducted

to evaluate the sensitivity and the sources of uncertainties in model predictions. Sensitivity simulations include those with and without heterogeneous reactions and those with different modules/algorithms for SOA formation, particle growth due to condensation (or shrinkage due to volatilization) and aqueous-phase chemistry as well as gas/particle mass transfer. CMAQ-MADRID was provided to EPA for public utilization in October 2002.

We describe in Section 2 the formulation of MADRID including the treatment of aerosol thermodynamics, dynamics and processes that govern the chemical composition and size distribution of PM in MADRID. These processes include new particle formation, condensational growth (or shrinkage by volatilization), and mass transfer between the bulk gas phase and PM. We describe in Section 3 the treatment of cloud processes (e.g., particle scavenging, aqueous-phase chemistry, and particle formation after cloud evaporation), heterogeneous reactions taking place at the surface of particles or droplets, and dry/wet deposition of particles and condensable organic species. The application of CMAQ-MADRID along with results from base and sensitivity simulations is presented in Section 4. Finally, the results are summarized along with discussions on further model improvements in Section 5.

2. FORMULATION OF MADRID

MADRID is developed to simulate important microphysical processes that govern the chemical composition and size distribution of PM. We conducted comprehensive reviews of existing modules available to simulate PM thermodynamics and dynamics [*Zhang et al.*, 1999, 2000; *Seigneur*, 2001]. Based on these reviews, a set of modules or algorithms that provides the best compromise between numerical accuracy and computational efficiency was selected to simulate those processes. The selected modules were then integrated and, if warranted,

modified, to constitute a coherent framework for the simulation of atmospheric PM. The formulation of MADRID is described below according to the major PM processes.

2.1 Chemical Composition of PM

PM consists of primary components that are emitted directly into the atmosphere and secondary components that are formed in the atmosphere by nucleation or condensation of gaseous species. We consider organic and inorganic PM of anthropogenic and biogenic origin. The chemical composition of PM is governed by the mass transfer between the bulk gas phase and the surface of the particles and the phase transition at the surface. The rate of mass transfer depends strongly on the composition at thermodynamic equilibrium between the bulk gas phase and the particles. The timescale for establishing thermodynamic equilibrium is sufficiently small for particles of small size; thermodynamic equilibrium between the gas phase and fine particles is therefore justified [e.g., *Meng and Seinfeld*, 1998; *Fahey and Pandis*, 2001]. The thermodynamic equilibrium cannot always be assumed for coarse particles (except for liquid water), however, and all other species are usually not in equilibrium. This complicates the aerosol modeling, as the dynamics of mass transfer have to be explicitly treated, at least for the larger particles with high concentrations. We describe below the treatment of gas-particle thermodynamics. The treatment of mass transfer under non-equilibrium conditions is described in Section 2.2.4.

2.1.1 Thermodynamics for inorganic species

A comprehensive review of the existing algorithms available to simulate the gas/particle thermodynamic equilibrium of inorganic species was conducted by *Zhang et al.* [2000] and updated as candidate algorithms underwent further improvements. Six modules

that simulate the gas/particle partitioning of inorganic species were compared using 400 different case studies. These six modules included MARS-A [*Binkowski and Shankar*, 1995], SEQUILIB [*Pilinis and Seinfeld*, 1987], SCAPE2 [*Kim and Seinfeld*, 1995; *Meng et al.*, 1995], EQUISOLV II [*Jacobson*, 1999], AIM2 [*Clegg et al*., 1998a, 1998b] and ISORROPIA [*Nenes et al.*, 1998; 1999]. All modules treat sulfate, nitrate, ammonium and water. Except for MARS-A, all modules also treat sodium and chloride. In addition, SCAPE2 and EQUISOLV II treat crustal soluble species: calcium, magnesium, potassium and carbonate. AIM2 does not simulate alkaline systems and was therefore not considered for incorporation into MADRID. MARS-A was the default module of CMAQ but it does not treat sodium chloride (NaCl). Among the computationally efficient modules that treat NaCl, ISORROPIA was judged superior to SEQUILIB in terms of numerical accuracy and stability. For a comprehensive treatment of the aerosol system, both SCAPE2 and EQUISOLV II were considered suitable. SCAPE2 is more computationally demanding than ISORROPIA (e.g., by factors of 10 to 440 under the conditions tested in *Nenes et al.* [1998]). EQUISOLV II can be applied to solve aerosol thermodynamic equilibrium at one time for either a single grid cell or multiple grid cells with a vectorized approach that can be applied to scalar or vector machines. We have tested the computational time of EQUISOLV II and ISORROPIA. For the tests, both modules consider the same total number of equilibrium equations but with different sets of equilibria, and ISORROPIA solved fewer equations in some concentration/relative humidity (RH) regimes. Under these test conditions, ISORROPIA required less computational time in a single grid cell than did EQUISOLV II for the same convergence criteria. As the number of grid cells increased, EQUISOLV II became more computationally efficient than ISORROPIA because the computer time required per grid cell decreases on a scalar machine due to an array-referencing minimization technique, and additional speedup occurs with multiple cells on a

vector machine due to vectorization [*Zhang et al.*, 2000]. However, it is not a trivial effort to implement the vectorized version of EQUISOLV II into CMAQ for solving aerosol thermodynamics at one time for multiple grid cells. Moreover, PM emission inventories do not yet include the chemical composition of crustal species that are treated in EQUISOLV II. Therefore, ISORROPIA was selected to simulate the thermodynamics of inorganic PM species in MADRID. The latest version of ISORROPIA (i.e., v1.6) is currently used in MADRID.

The thermodynamic equilibria that are simulated by ISORROPIA are presented by *Nenes et al.* [1998]. The entire concentration domain is divided into subdomains such as sulfate very-rich (free acid), sulfate rich (non free acid), sulfate poor and sodium poor, and sulfate poor and sodium rich. The systems of non-linear equations for each subdomain were ordered and manipulated so that analytical solutions can be obtained for as many equations as possible. Adopting this approach, most cases can be solved using only one level of iteration, which increases computational efficiency considerably. Significant speedup is also obtained by minimizing the number of calls to subroutines that calculate activity coefficients. In addition, some speedup can be gained under some conditions by reducing the number of equations solved for a given RH/concentration regime and/or using pre-calculated activity coefficient tables. The bisection method is used to obtain the solution. ISORROPIA provides options to treat particles to be either in a thermodynamically stable state, where particles can be solid, liquid or both, or in a metastable state, where particles are always an aqueous solution. The first option (i.e., all states are treated) is used in MADRID.

2.1.2 Thermodynamics for organic species

Accurate simulation of SOA formation requires a gas-phase mechanism that treats all important semivolatile or nonvolatile organic species and their oxidation products. Such a

detailed representation of organic species and their chemistry, however, usually can not be incorporated in 3-D air quality model, due mainly to computational constraints and current knowledge gaps in the atmospheric chemistry of organic compounds. Different VOC-lumping approaches are therefore used in existing gas-phase chemical mechanisms to provide a simplified treatment for VOC speciation and chemistry. These include the lumped structure approach (e.g., the Carbon-Bond Mechanism Version IV (CBM-IV) of *Gery et al.* [1989]); the lumped species approach (e.g., the Regional Acid Deposition Mechanism Version 2 (RADM2) of *Stockwell et al.* [1990] and the Statewide Air Pollution Research Center gas-phase mechanism (SAPRC-99) of *Carter* [2000]); and the lumped surrogate species (e.g., the Caltech Atmospheric Chemistry Mechanism (CACM) of *Griffin et al.* [2002]). CACM contains 361 reactions of 191 species and provides detailed descriptions of several generations of products from alkanes (3 classes), alkenes (2 classes), aromatics (2 classes), alcohols (3 classes), isoprene and terpenes (2 classes) [*Griffin et al.*, 2002]. This mechanism is uniquely suitable for simulating SOA formation because it explicitly treats 42 condensable second- and third-generation products. Although many of the reactions for organic species are generalized and some organic species are non-explicit, SAPRC-99 includes the product yield coefficients and rate constants for over 100 individual organic species [*Carter*, 2000]. It is, therefore, suitable for simulating SOA formation. Its predecessors (i.e., SAPRC-90, SAPRC-93 and SAPRC-97) have been applied for simulating SOA formation in several airsheds [e.g., *Pandis et al.*, 1992, 1993; *Bowman et al.*, 1995]. SAPRC-99 is available in Models-3/CMAQ since June 2002. On the other hand, both CBM-IV and RADM2 are computationally more efficient than both CACM and SAPRC-99. They contain only a few explicit and lumped organic species, thus, they may not be well suited for a detailed representation of SOA formation. For example, since individual organic compounds are lumped based on carbon-bond structure in CBM-IV,

they are often disaggregated and assigned to more than one mechanism species. Many of the organic mechanism species thus contain fragments of molecules and the identity of the original organic compound is lost. It is therefore not possible to track the amount of some SOA precursors (e.g., long-chain alkanes and alkenes) reacting in CBM-IV.

CMAQ-MADRID includes two SOA formulations: one uses an empirical representation of SOA formation (referred to as MADRID 1) that is based on data obtained in smog chamber experiments [*Odum et al.*, 1997; *Griffin et al.*, 1999]; the other uses a mechanistic representation of SOA formation (referred to as MADRID 2) that simulates an external mixture of hydrophilic and hydrophobic particles [*Pun et al.*, 2002]. Different gas-phase chemical mechanisms are used in MADRID 1 and MADRID 2 to accommodate the different SOA speciations simulated. MADRID 2 uses CACM gas-phase chemistry. MADRID 1 uses either CBM-IV or RADM2, which are the only two gas-phase chemical mechanisms available in the August 2000 version of Models-3/CMAQ. MADRID 2 includes 10 surrogate compounds, grouped according to their affinity for water (5 surrogate species for 28 explicit hydrophobic compounds and 5 surrogate species for 14 hydrophilic compounds), origin (anthropogenic vs. biogenic), size (number of carbons), volatility, and dissociation properties [*Pun et al.*, 2002]. Hydrophilic organic compounds include those with a short carbon chain ($\leq$ 7 carbons; or $\leq$ 10 carbons with three or more functional groups), high solubility ($\geq$ 1 g solute / 100 g water), and a high effective Henry's law constant ($\geq 1 \times 10^6$ M atm^{-1}). Hydrophobic compounds are identified by their estimated octanol-water partition coefficients. A detailed description of MADRID 2 has been presented elsewhere [*Pun et al.*, 2002] and is not repeated here. For MADRID 1, the formulation of the SOA module requires some additional precursors and condensable organic products that are not explicitly treated in CBM-IV or RADM2 (a detailed list of SOA precursors and products used in CBM-IV and

RADM2 can be found in Byun and Ching [1999]). Therefore, it is necessary to add several organic species and reactions to these two mechanisms to make them compatible with the SOA formulation of MADRID 1. *Zhang et al.* [2002a] and *Pun et al.* [2003] have presented the chemical speciation used for the formulation of MADRID 1. We present below the SOA formulation in MADRID 1, along with modifications to the original CBM-IV and RADM2 gas-phase chemical mechanisms.

The MADRID 1 formulation for SOA includes 2 anthropogenic VOC precursors, 4 surrogate anthropogenic species representing their condensable products, 12 biogenic VOC (BVOC) precursors and 34 surrogate biogenic species representing their condensable products (22, 8 and 4 surrogate species resulted from the OH, O_3 and NO_3 oxidation reactions, respectively). The two anthropogenic precursors are assumed to be aromatics and are characterized as one with low SOA yield and one with high SOA yield. The high-yield aromatic species include those containing no more than one methyl substituent and no more than one ethyl substituent (i.e., toluene, ethylbenzene and ethyltoluenes) as well as *n*-propylbenzene. The low-yield aromatic species include those containing two or more methyl substituents (i.e., xylenes, trimethylbenzenes, dimethylethylbenzenes and tetramethylbenzenes). The existing CBM-IV and RADM2 lumped aromatic species toluene (TOL) and xylene (XYL) represent aromatics with 7- and 8-carbon ring structures in CBM-IV or less and more reactive aromatics in RADM2, respectively. These two lumped species (i.e., TOL and XYL) were selected to represent the high-yield and low-yield anthropogenic precursors, respectively. Other anthropogenic SOA precursors, such as long-chain (> C8) alkanes, long-chain internal alkenes and cresol and phenols, are not considered in MADRID 1 (they are treated in MADRID 2). Four anthropogenic condensable products were added to the existing reactions of TOL and XYL: TOLAER1 and TOLAER2 (high aerosol yield products)

for TOL oxidation by OH and XYLAER1 and XYLAER2 (low aerosol yield products) for XYL oxidation by OH, using the experimentally-determined stoichiometric coefficients of *Odum et al.* [1997]. The 12 biogenic precursors in MADRID 1 do not appear explicitly in CBM-IV and RADM2 because they are decomposed into their functional groups (i.e., ALD2, OLE and PAR) in CBM-IV or assigned to surrogate species in RADM2. Therefore, we added those species and their corresponding oxidation reactions which lead to biogenic SOA (BSOA) formation using the experimentally-determined stoichiometric coefficients of *Griffin et al.* [1999] and the kinetic rate constants compiled in *Lamb et al.* [1999].

Since BVOC are already represented in the original lumped structure (or species) formulation of CBM-IV (or RADM2) to simulate O_3 formation, it is important that the reactions added for BSOA formation do not alter O_3 chemistry. Accordingly, we added oxidation reactions of BVOC in a format such that an oxidant (e.g., OH, O_3 and NO_3) is treated as both a reactant and a product following the approach of Gipson and Young (1999), namely:

$$BVOC + OH \rightarrow b\ BSOA + OH$$

where b is the stoichiometric coefficient for the biogenic product BSOA. In this way, the oxidant mixing ratio and thus O_3 chemistry are unaffected by this new reaction, which affects only the precursor and the condensable organic product.

The following equation governs the gas/particle partitioning of each of the condensable species in MADRID:

$$K_i = \left(\frac{A_i / M_{sum}}{G_i}\right) \qquad (1)$$

where K_i (m^3 μg^{-1}) is the partition coefficient obtained from the smog chamber experiments, A_i and G_i (μg m^{-3} air) are the mass concentrations of species *i* in the particulate- and gas-phase, respectively, and M_{sum} (μg m^{-3} air) is the sum of primary organic carbon (OC) (non-volatile) and secondary OC (semi-volatile) in the particulate phase that serve as the organic absorbing medium. The SOA yields and gas/particle partition coefficients at experimental temperatures are based on *Odum et al.* [1997] and *Griffin et al.* [1999]. *Griffin et al.* [1999] conducted outdoor chamber experiments on aerosol formation under both daytime conditions in the presence of OH, O_3 and NO_3 and nighttime conditions with either O_3 or NO_3. Since the OH radical is the primary oxidant that oxidizes the largest fractions of BVOC during the daytime [*Griffin et al.*, 1999], we assume that the 22 surrogates from the daytime photooxidation experiments of *Griffin et al.* [1999] resulted from the OH oxidation. The daytime SOA yields and gas/particle partition coefficients from *Griffin et al.* [1999] are thus used for these OH oxidation reactions in MADRID 1.

The smog chamber experiments from which K_i and stoichiometric coefficients were derived were conducted at temperatures higher (301-316 K) than the typical ambient temperatures. Following *Sheehan and Bowman* [2001], the temperature dependence of K_i can be accounted for as follows:

$$K_i(T) = K_i^* \frac{T}{T^*} \exp\left[\frac{\Delta H_{vap,i}}{R}\left(\frac{1}{T} - \frac{1}{T^*}\right)\right] \qquad (2)$$

where $K_i(T)$ and K_i^* are the partition coefficients at temperature *T* and a reference temperature T^*, respectively. *R* is the ideal gas constant (8.2 x 10^{-5} m^3 atm mol^{-1} K^{-1}). $\Delta H_{vap,\,i}$ is the enthalpy of vaporization of the pure species *i*. The value of $\Delta H_{vap,\,i}$ is assumed to be 88 kJ $mole^{-1}$ for condensable products from terpenes and aromatics (< C10) and 175 kJ $mole^{-1}$ for

those from sesquiterpenes. The values for $\Delta H_{vap,\ i}$ correspond to the arithmetic mean of available literature data for < C10 and > C10 compounds [*Tao and McMurry*, 1989; *Bilde and Pandis*, 2001].

2.2 Aerosol Dynamics

2.2.1 Particle size distribution

Two major approaches have been commonly used to represent the particle size distribution: the modal and the sectional approaches. In the modal approach, the particle size distribution is represented by several modes (e.g., Aitken, accumulation and coarse modes) and an analytical function (typically, a lognormal distribution) is used to represent the particle size distribution of each mode. The aerosol dynamic processes that govern the evolution of the particle size distribution can then be solved analytically. In the sectional approach, the particle size distribution is approximated by a discrete number of size sections. Some properties of the particle size distribution (e.g., mass of individual chemical species) are then assumed to be uniform within each size section and to be conserved as the aerosol general dynamic equation is solved. The modal approach offers computational advantages over the sectional approach, but has inherent limitations in representing a wide variation of the observed aerosol size distributions and their physical and chemical processes (e.g., *Zhang et al.*, 2002b). The modal approach is used in the original CMAQ. The sectional approach is used in MADRID to represent the particle size distribution. The processes that govern aerosol dynamics include coagulation, nucleation (i.e., the formation of new particles), growth due to condensation (or shrinkage due to volatilization) and the mass transfer of chemical species between the bulk gas phase and the particle surface. All processes except for coagulation are treated explicitly in MADRID. Coagulation is not included in the current version of MADRID, although it may

have a large effect on fine particle number concentrations, particularly near emission sources, and it may affect the mass and number concentrations of fine particle via internally mixing particles over the entire size distribution [*Jacobson,* 2002]. For this particular study with a simulation period of a few days, the effect of neglecting coagulation on the overall PM mass predictions may be negligible, because the time scale for coagulation is long compared to that of other processes such as condensation. We do not attempt to evaluate the predicted PM number concentrations in this study, because coagulation may have a significant impact on fine particle number concentrations, the predicted PM number concentrations for ultra-fine particles (i.e., those with a diameter less than 0.1 μm) may not be accurate.

Either two or multiple particle size sections can be used to represent the particle size distribution in MADRID. For the 2-section representation (i.e., fine and coarse), particle growth by condensation and shrinkage by volatilization are not simulated because there is minimal exchange via growth/shrinkage between the fine and coarse particle sections. For a multi-sectional representation, a minimum number of 8 sections is recommended to provide sufficient resolution of particle sizes for the meaningful simulation of aerosol dynamic processes. New particle formation, growth by condensation, shrinkage by volatilization and gas/particle mass transfer are simulated. We describe below the formulations used in MADRID to simulate these processes.

The general dynamic equation for the multi-sectional representation of PM can be expressed as follows.

$$\frac{\partial q_i(d_{p,j},\boldsymbol{x},t)}{\partial t} = -\boldsymbol{u}(\boldsymbol{x},t)\bullet\nabla q_i(d_{p,j},\boldsymbol{x},t)$$

$$+\nabla\bullet(\boldsymbol{K}(\boldsymbol{x},t)\nabla q_i(d_{p,j},\boldsymbol{x},t) + V_d(\boldsymbol{x},t)\nabla q_i(d_{p,j},\boldsymbol{x},t)$$

$$+H_i(d_{p,j},\boldsymbol{x},t)\ q(d_{p,j},\boldsymbol{x},t) - \frac{\partial(m\,q_i(d_{p,j},\boldsymbol{x},t)\,H)}{\partial m} \qquad (3)$$

$$+E_i(d_{p,j},\boldsymbol{x},t) + F_i(d_{p,j},\boldsymbol{x},t)$$

where q_i is the mass of species i in size section j with a characteristic diameter $d_{p,j,}$ $\boldsymbol{x}$ is the position vector of the corresponding grid cell, t is the time, $\boldsymbol{u}$ is the resolved wind vector, $\boldsymbol{K}$ is the eddy-diffusivity tensor, V_d is the vertical deposition velocity that includes gravitational settling, H_i is the condensational growth rate, m is the mass of particles with a diameter $d_{p,j}$, E_i is the emission rate of particulate species i in size section j and F_i is the rate of new particle mass formation for species i in the lowest size section.

The first two terms on the right-hand side are solved using the host model transport algorithms [*Byun and Ching*, 1999]. The other terms are discussed below. Note that MADRID uses the Stokes particle diameter in its formulation whereas the $PM_{2.5}$ and PM_{10} regulations use the aerodynamic diameter. These two diameters are related by the square root of the particle density. For example, for a particle density of 1.35 g cm^{-3}, the aerodynamic diameter of 2.5 μm corresponds to a Stokes diameter of 2.15 μm.

2.2.2 Formation of new particles

Four algorithms [*Pandis et al.*, 1994; *Wexler et al.*, 1994; *Fitzgerald et al.*, 1998; *Harrington and Kreidenweis*, 1998] currently used in 3-D air quality models to calculate the absolute rate of particle nucleation were compared by *Zhang et al.* [1999]. Although all

algorithms were formulated from the same theoretical basis, they gave highly variable results under typical conditions. Therefore, the use of these parameterizations of the absolute nucleation rates is associated with significant uncertainties at present. Consequently, *Zhang et al.* [1999] recommended a method that calculates the relative rates of new particle formation and condensation on existing particles [*McMurry and Friedlander,* 1979] instead of calculating the absolute rate of nucleation. This method was selected for the treatment of new sulfate particle formation in MADRID.

The new particle parameterization of *McMurry and Friedlander* [1979] is computationally demanding because it involves iteration among several equations. Consequently, a parameterized version that uses a look-up table with precalculated rates of new particle formation is used. An option for neglecting the calculation of new particle mass formation is also provided.

2.2.3 Condensational growth

Condensational growth (or shrinkage due to volatilization) is a process that allows particles to grow (or shrink) upon condensation of the condensable species (or evaporation of the volatile species). The simulation of condensation/volatilization is challenging with a sectional representation because numerical diffusion may result from the solution of the governing equation in 3-D simulations. Three basic approaches have been used to simulate condensational growth:

(1) Semi-Lagrangian techniques that calculate the mass (or number) flux from one section to the next. The basic finite-difference method [e.g., *Seigneur,* 1982] is the simplest example of a semi-Lagrangian technique. Bott's scheme [*Bott,* 1989], the

scheme of *Chock and Winkler* [2000] and that of *Nguyen and Dabdub* [2002] are more advanced examples of semi-Lagrangian techniques.

(2) Lagrangian techniques that calculate the movement of the section boundaries according to the growth law and redistribute the resulting sectional distribution onto the fixed sectional representation. The UAM-AERO scheme [*Lurmann et al.*, 1997] is an example of a Lagrangian technique where a spline function is used for the redistribution of the sectional representation.

(3) The moving-center technique of Jacobson [*Jacobson*, 1997a] where the diameter representative of the section moves according to the growth law. It contains features of both Eulerian and Lagrangian schemes, since it uses fixed boundaries and allows movement within and across the boundaries.

Zhang et al. [1999] compared four condensational growth algorithms: one modal approach that is used in Models-3/CMAQ [*Binkowski and Shankar*, 1995] and three sectional approaches: the Bott's scheme used in the 1998 version of the CIT model [*Meng et al.*, 1998], the UAM-AERO scheme and the moving-center scheme. The Bott's and the UAM-AERO schemes were shown to lead to significant numerical diffusion and the moving-center scheme appeared to be the most accurate among the algorithms tested. Consequently, the moving-center scheme is used to simulate condensational growth in MADRID with more than two particle size sections. The sensitivity of the predicted total particle mass and size distributions to the moving-center scheme and a simple finite-difference scheme are evaluated in the sensitivity study.

The following growth law is used in MADRID to simulate the flux between the gas phase and particles [*Capaldo et al.*, 2000],

$$J_{i,j} = 2\pi d_{p,j} D_{g\,i}\, N_j \left(C_{\infty,i} - C_{s\,i,\,j}\right) \frac{1+K_{n_{i,j}}}{1+2\,K_{n_{i,j}} \dfrac{\left(1+K_{n_{i,j}}\right)}{\alpha_{i,j}}} \qquad (4)$$

where $J_{i,j}$ is the growth/evaporation rate of species i in a particle in size section j, N_j is the number density of particles in section j, D_{gi} is the molecular diffusivity of species i in air, $C_{\infty,i}$ and $C_{si,j}$ are the concentrations of species i in the bulk gas phase and at the surface of particles in section j, respectively. $K_{ni,j}$ is the Knudsen number, $K_{ni,j} = 2\,\lambda_i/d_{p,j}$, λ_i is the mean free path of species i, and $\alpha_{i,j}$ is the accommodation coefficient for species i on the particle in section j, a value of $\alpha_{i,j} = 0.1$ is assumed for all species and all size sections.

Each section center (i.e., $d_{p,j}$) moves according to the change in mass in the section. As a section center reaches one of the boundaries of the section (upper boundary in the case of condensation; lower boundary in the case of volatilization), the particulate mass contained in that section moves into the adjacent section. This technique minimizes numerical diffusion across size sections since particulate mass is transferred from one section to the next only in the case where a section center reaches one of the section boundaries. It is important to note that this technique allows the simultaneous tracking of PM mass and number concentrations. In the most common implementation of the sectional approach in 3-D models, only PM mass is tracked, PM number is generally not conserved, since the PM number concentrations are diagnosed from the predicted PM mass and the fixed PM mean diameters (i.e., the so-called single-moment algorithm).

In a 3-D air quality model, PM populations that are mixed within a given grid cell are likely to originally have different section centers. We used a mixing approach that is similar to that of *Jacobson* [1997a] for mixing PM populations within a given grid cell via advection,

turbulent diffusion, convection, emissions and sedimentation. In this approach, an initial particle size distribution is assumed for newly-emitted particles to calculate the number concentrations of the emitted particles based on the emitted mass concentrations. The emitted particles are then placed in the section surrounding their diameter. Since the changes in both mass and number concentrations of particles due to various atmospheric processes (e.g., emission, advection, turbulent diffusion and nucleation) are explicitly treated in CMAQ-MADRID, the new common section center for the mixed particles in a given size section can then be calculated using the particle mass and number concentrations (m_j and n_j, respectively) in the same size section:

$$d_{p,j} = \sqrt[3]{\frac{6m_j}{\pi \cdot n_j \cdot \rho_p}} \tag{5}$$

where ρ_p is the density of the particle.

2.2.4 Gas/particle mass transfer

Gas/particle mass transfer is a process that transfers mass of condensable species from bulk gas phase to the particle surface. The time scale for the diffusion of a molecule from the bulk gas phase to the surface of a particle increases with the diameter of the particle. Therefore, fine particles will tend to reach equilibrium rapidly whereas coarse particles can remain in non-equilibrium conditions [e.g., *Wexler and Seinfeld*, 1990; *Dassios and Pandis*, 1999]. Three basic approaches have been developed to treat the gas/particle mass transfer:

(1) Dynamic approach that explicitly simulates gas/particle mass transfer for each size section by solving the equation for mass fluxes between the bulk gas-phase and individual particles (or particles in a given size range). Chemical concentrations in the bulk gas phase and in the particles in a given size section may or may not be in equilibrium. Examples of the dynamic approaches for multicomponent aerosols include those of *Meng et al.* [1996, 1998], *Jacobson* [1997a, 1997b], *Sun and Wexler* [1998 a, 1998b] and *Pilinis et al.* [2000].

(2) Equilibrium approach that assumes an instantaneous chemical equilibrium between the bulk gas phase and the whole particulate phase. This approach can be further divided into two categories: bulk equilibrium approach and non-bulk equilibrium approach. In the bulk equilibrium approach, all particles over size sections are assumed to have the same chemical composition. In the non-bulk equilibrium approach (also referred to as the size-resolved equilibrium approach, see *Moya et al.*, 2002), particles in different size sections may have different chemical compositions. The bulk equilibrium approach of *Binkowski and Shankar* [1995] and the simple bulk equilibrium approach of Hudischewskyj and Seigneur [1989] and Seigneur et al. [1997] (the latter approach was used in the sensitivity study in this work and is referred to as a simple bulk equilibrium approach hereafter) are examples of simple bulk equilibrium approaches, in which the transferred material is allocated to the particle size distribution using weighting factors that are derived based on either initial particle mass/surface area or a given distribution. In more advanced bulk equilibrium approaches such as those used in UAM-AERO [*Lurmann et al.*, 1997] and CIT [*Meng et al.*, 1998] (the latter approach is referred to as the CIT bulk equilibrium hereafter), the weighting factors are calculated based on condensational growth law using diffusion-limited assumptions,

accounting more or less for the non-equilibrium between the bulk gas phase and particles in a given size range. Examples of non-bulk equilibrium approach include those of *Pilinis and Seinfeld* [1987]; *Kleeman et al.* [1997]; *Jacobson et al.*, [1996]; *Jacobson* [1999] and *Moya et al.* [2002], in which a system of non-linear algebraic equations is solved for each size range to determine the partitioning of semi-volatile species, while the mass transfer between the bulk gas-phase and bulk particulate phase is still considered to occur at an instantaneous thermodynamic equilibrium.

(3) Hybrid approach that combines both dynamic and equilibrium approaches. The CMU hybrid approach of *Capaldo et al.* [2000] is an example of such a hybrid approach, in which the mass transfer is treated explicitly for the coarse particles and the gas/particle equilibrium is assumed for the fine particles.

The dynamic approach provides the most accurate representation of interphase partitioning of semi-volatile species in theory but its use in 3-D air quality models is limited by its large computational expenses. In the dynamic approaches that are used in current 3-D models (e.g., CIT, GATOR and UAM-AIM), particles are usually assumed to be internally mixed (i.e., all particles within a given size range have the same chemical composition) and are distributed according to size sections. Therefore, the mass transfer equation is solved between the bulk gas phase and the surface of the particles. On the other hand, the equilibrium approach is computationally efficient and has been used extensively in many 3-D models. *Zhang et al.* [1999] compared the CIT bulk equilibrium approach and the simple bulk equilibrium approach with the CIT dynamic approach in a box model. They found that the simple bulk equilibrium approach is inaccurate under many ambient conditions, whereas the CIT bulk equilibrium approach is appropriate when chloride and carbonate concentrations are

insignificant. While the bulk equilibrium approach introduces errors in the partitioning calculation, particularly for cases with highly reactive coarse particles, the non-bulk equilibrium approach provides a more accurate representation of the interphase partitioning. However, the non-bulk equilibrium approach may lead to infinite solutions for solids and the equilibrium assumption is usually not valid for coarse particles. The novel hybrid approach combines merits of both dynamic and equilibrium approaches, therefore, it provides the best compromise between numerical accuracy and computational speed. Accordingly, we selected the hybrid approach of *Capaldo et al.* [2000] (referred to as the CMU hybrid approach) to treat gas/particle mass transfer in MADRID and modified it as discussed below.

Capaldo et al. [2000] recommended the use of a threshold size of 1 μm, which is a cut-off size between the equilibrium approach and the dynamic approach. We tested a threshold of 2.15 μm under typical urban aerosol conditions in a box model to estimate the sensitivity of model results to the selection of the cut-off size. The maximum difference in predicted PM concentrations in a given size section with the two thresholds under the tested conditions was only 3%, although errors in predicted size distribution may be higher under other conditions or small errors may propagate into larger errors over long simulation periods in a 3-D model. Nevertheless, a threshold value of a Stokes diameter of 2.15 μm represents a suitable compromise between computational efficiency and accuracy and is, therefore, used when 2 or 8 size sections are selected in MADRID. For a different section number and/or distribution, a cut off size between 1 and 2.15 μm should be selected by the user to be the threshold value.

For particles in size sections above the threshold diameter, the mass transfer flux equation is solved according to the growth law of Equation 4. The chemical concentration $C_{si,j}$ is calculated by solving the gas/particle thermodynamic equilibrium knowing the particulate chemical concentrations. This calculation is conducted using ISORROPIA for wet particles

and the Multicomponent Aerosol Dynamic Model (MADM) for dry particles [*Pilinis et al., 2000*; *Capaldo et al.,* 2000]. If the bulk gas-phase chemical concentration exceeds the concentration at the surface of the particle, the mass transfer occurs from the bulk gas phase toward the particle, and vice-versa. The mass transfer and thermodynamic equilibrium equations are solved iteratively until convergence is attained.

For particles in size sections below 2.15 μm in diameter, mass transfer is assumed to be instantaneous:

$$C_{si,j} = C_{\infty,i} \tag{6}$$

Thus, ISORROPIA is used to calculate the bulk particulate concentrations given the bulk gas-phase concentrations. The material transferred between phases is distributed over the fine particle size sections by using weighting factors that are based on the surface area of particles in each section [*Capaldo et al.,* 2000].

As chemical species either condense onto or volatilize from the particles, these particles grow or shrink accordingly. Therefore, in the case where more than 2 sections are selected, the hybrid mass transfer algorithm must be coupled with a growth/shrinkage algorithm. The original formulation of the mass transfer algorithm in the CMU hybrid approach used a finite-difference scheme to treat growth/shrinkage of the particles. As discussed above, such schemes can lead to substantial numerical diffusion. Therefore, the finite-difference scheme was replaced by the moving-center scheme described above.

CMAQ-MADRID offers two other options for gas-to-particle mass transfer: a simple bulk equilibrium approach in which Equation 6 applies to all size sections and the weighting factors are calculated based on particulate sulfate concentrations; and the CIT bulk equilibrium

approach of *Meng et al.* [1998]. The CIT bulk equilibrium approach distributes the particle mass changes over the size sections based on a particle surface area weighting that is similar to that of the CMU hybrid approach. These two options are computationally more efficient than the CMU hybrid approach. The sensitivity of the predicted particle mass concentrations and size distribution to the three different gas/particle mass transfer approaches is presented in Section 4.5.4.

3. FORMULATION OF OTHER PROCESSES RELATED TO PM

Besides the processes that directly govern the chemical composition and size distribution of PM, other processes that also affect PM size distributions must be considered. Such processes include cloud processes that lead to additional PM mass via aqueous-phase reactions in cloud droplets and subsequent evaporation; heterogeneous reactions at the surface of cloud droplets and particles that produce additional PM; and deposition processes that remove particles of different sizes. We describe the modifications that were made to CMAQ to account for those additional processes in conjunction with the incorporation of MADRID into CMAQ.

3.1 Cloud Processes

The original CMAQ cloud module was modified to include a more comprehensive aqueous-phase chemical mechanism and to provide treatment of cloud processing of aerosols (e.g., particle activation and scavenging, particle formation from droplet evaporation) that is based on a sectional size representation. We describe these modifications below.

3.1.1 Aqueous-phase chemistry

The original CMAQ includes a simplified aqueous-phase chemical mechanism that is based on the RADM mechanism [*Walcek and Taylor*, 1986]. It includes only 10 gas-aqueous equilibria, 9 aqueous equilibria and 5 kinetic reactions for the oxidation of SO_2 to sulfate. Because the solubility of SO_2 and the oxidation rates of dissolved SO_2 species depend on the acidity of the cloud or fog droplet, the aqueous-phase chemical mechanism needs to include a fairly long list of species that can affect the acidity of atmospheric droplets. The requirements for such an aqueous-phase chemistry module are (1) a robust and efficient numerical solver and (2) a relatively complete representation of the aqueous chemistry of sulfur and nitrogen species. We selected a more comprehensive chemical kinetic mechanism, i.e., the CMU bulk aqueous-phase chemical mechanism [*Pandis and Seinfeld*, 1989; *Seinfeld and Pandis*, 1998; *Fahey and Pandis*, 2001] and incorporated it as an option into CMAQ. The CMU mechanism includes 17 gas-aqueous equilibria, 17 aqueous equilibria, and 99 aqueous-phase kinetic reactions among 18 gas-phase species and 27 aqueous-phase species. Like all available aqueous-phase mechanisms, it is designed to simulate sulfate production from SO_2 in atmospheric liquid water and includes the three dominant oxidation pathways for S[IV] by H_2O_2, O_3, and O_2 catalyzed by Fe^{3+} and Mn^{2+}. In addition, it includes other reactions for the oxidation of S[IV] to sulfate, the oxidation of nitrogen species to nitrate, and reactions for carbonate, chlorine, organic and oxygen species that are involved in the formation of sulfate and/or nitrate species.

The mechanism was implemented with options that allow the user to reduce the number of aqueous-phase chemical reactions used in a particular simulation. The user can include or exclude (1) the chlorine chemistry, (2) the radical chemistry, and (3) the Fe^{3+} and Mn^{2+} catalyzed oxidation of dissolved SO_2. These options are provided because these portions of the chemistry may have only small effects on the results and sometimes present very stiff

numerical conditions that require significant amounts of computer time. Neglecting the radical chemistry in polluted environments improves computational efficiency without introducing significant errors. The concentrations of radical species (i.e., OH, HO_2, O_2^-, NO_3, $ClOH^-$, SO_4^- and CO_3^-) become zero in the aqueous phase when the radical chemistry is turned off. In this case, the CMU mechanism consists then of 14 gas-aqueous equilibria, 16 aqueous equilibria, and 32 aqueous kinetic reactions among 18 gas-phase species and 19 aqueous-phase species.

3.1.2 Aerosol activation and scavenging

Aerosol activation and scavenging contribute to the species concentrations in cloud droplets. The activated or scavenged fraction is influenced by many factors including the types of clouds, cloud supersaturation, the characteristics of aerosols (e.g., number concentration, size distribution, chemical composition and solubility), and updraft velocity. Both empirical and mechanistic parameterizations have been used to simulate aerosol activation by cloud droplets in 3-D models. In the interest of computational efficiency, we developed an empirical parameterization for the sectional size representation based on available observations, as shown in Table 1.

For a relatively fine resolution of the particle size representation (i.e., 6 or more size sections between 0.02 and 10 μm), particles with aerodynamic diameter greater than 0.35 μm are assumed to be 100% activated (this diameter corresponds to a Stokes diameter of 0.3 μm for a density of 1.35 g cm^{-3}). The use of 0.35 μm as an activation cutoff diameter is a reasonable approximation because particles larger than this size are estimated to require a supersaturation less than 0.03% for activation, a prevailing condition for most clouds [*Gillani et al.*, 1995]. Note that a larger activation cutoff diameter may be needed for episodes with heavy fogs. For example, few particles smaller than 1 μm are activated by fogs (because of

much smaller supersaturations) in Los Angles or San Joaquin Valley of California. Particles with aerodynamic diameter greater than 0.1 μm (i.e., a Stokes diameter of 0.086 μm for a density of 1.35 g cm^{-3}) but smaller than 0.35 μm are assumed to be partially activated. Both observations and theoretical calculations have shown that the fraction of activation for particles in this size range can vary from 0 to 1 [e.g., *Gillani et al.*, 1995; *Leaitch*, 1996; *Liu et al.*, 1996]. We assume that 50% of the particle mass in this size range is activated completely into cloud droplets, and that the remaining 50% of particle mass is slowly scavenged according to $exp(-\beta \tau)$, where β is the mass (or number) scavenging coefficient for particle in the size range of 0.1-0.35 μm. It is determined by simulated cloud properties (e.g., droplet size distribution, liquid water content and settling velocity) and aerosol properties (e.g., particle size distribution and polydisperse diffusivity) based on the equation of *Pruppacher and Klett* [1980] [*Binkowski*, 1999]. τ is the cloud chemistry timestep for grid-resolved cloud and the cloud lifetime for subgrid convective clouds. A 1-hr lifetime is assumed for subgrid convective clouds [*Byun and Ching*, 1999]. Particles with aerodynamic diameter less than 0.1 μm are assumed to remain as interstitial particles with 0% activated. For a coarse size resolution (i.e., 2 to 5 size sections between 0.02 and 10 μm), an activation cutoff diameter of 2.5 μm is used and the activated fraction for particles smaller than 2.5 μm is assumed to be 80%.

3.1.3 Formation of particles after cloud evaporation

The particle concentrations after cloud evaporation are calculated as follows. The change in mass concentration of individual particulate components during the cloud lifetime (i.e., between cloud formation and evaporation) is calculated first. This change is then added to the activated particle size distribution using a uniform relative change across the particle size distribution. For example, if the total change in sulfate concentration is a 10% increase, the

sulfate concentrations in each particle size section are increased by 10%. The activated mass along with its changes due to aqueous-phase chemistry is then added back to the interstitial mass size distribution to obtain the total particle mass size distribution after cloud evaporates.

If a 2-section particle size representation is used, no particle mass movement is simulated between the 2 size sections. For a multi-section particle size representation, however, it is necessary to account for particle growth that occurs due to the increase in mass in each size section. The moving-center scheme is used to calculate the new particle size distribution that results from this particulate mass increase.

3.2 Heterogeneous Chemistry

Jacob [2000] conducted a review of heterogeneous chemistry and recommended that the heterogeneous reactions of HO_2, NO_2, NO_3 and N_2O_5 on the surface of aqueous particles and cloud droplets be parameterized by a simple reaction probability in 3-D O_3 models. In this parameterization, the uptake of a gas-phase species by condensed phases is considered as an irreversible loss process with a first-order heterogeneous reaction rate constant. Based on *Jacob* [2000], we consider the following heterogeneous reactions on the surface of aqueous particles or cloud/fog droplets in CMAQ-MADRID:

$$HO_2 \xrightarrow{PM} 0.5H_2O_2 \qquad (R1)$$

$$NO_2 \xrightarrow{PM} 0.5HONO + 0.5HNO_3 \qquad (R2)$$

$$NO_3 \xrightarrow{PM} HNO_3 \qquad (R3)$$

$$N_2O_5 \xrightarrow{PM} 2HNO_3 \qquad (R4)$$

$$N_2O_5 \xrightarrow{Cloud\ /\ Fog} 2HNO_3 \qquad (R5)$$

Recent experimental data suggest that bulk aqueous-phase chemistry is consistent with the rate of the reaction of NO_2 in presence of condensed water [*Cheung et al.*, 2000]. Following discussions with *Jacob* [*D. Jacob*, Harvard University, personal communication, 2001], we elected not to include the heterogeneous reaction of NO_2 on droplets; it is, however, included in the CMU bulk aqueous-phase mechanism. In addition, the heterogeneous reactions of HO_2 and NO_3 on droplets were not included, since the bulk CMU aqueous-phase mechanism already includes the scavenging of HO_2 and NO_3 by cloud droplets and their subsequent aqueous-phase equilibria and reactions. The first-order rate constant, *k*, for the heterogeneous loss of a gaseous species *i* to the condensed phase is calculated following *Jacob* [2000]:

$$k_i = \left(\frac{a}{D_{gi}} + \frac{4}{\nu_i \gamma_i}\right)^{-1} A \qquad (7)$$

where *a* is the radius of particles or cloud/fog droplets, D_{gi} and ν_i are the gas-phase molecular diffusion coefficient and the mean molecular speed, respectively, of a gaseous species *i* in air, γ is the reaction probability of species *i*, which represents the likelihood that a gas molecule impacting the surface of the condensed phase will undergo reaction, and *A* is the surface area of the condensed phase. For atmospheric particles, *A* is obtained by integrating over the particle size distribution. The first term on the right-hand side of Equation 7 represents the uptake by diffusion from the bulk gas phase to the surface of the condensed phase and the second term represents the uptake by free molecular collisions of gas molecules with the surface. If $k_i \rightarrow (D_{gi} A/a)$ (e.g., R1), the uptake of a gas molecule by the condensed phase is diffusion-limited and shows little dependence on the value of γ_i. On the other hand, if $k_i \rightarrow (\nu_i \gamma_i A/4)$ (e.g., R2 and R3), the uptake of a gas molecule tends to be limited by free molecular

collision and depends strongly on the magnitude of γ_i. The uptake of species like N_2O_5 can be either fully diffusion-limited (e.g., on cloud droplets with diameter greater than 20 μm and γ_i = 0.1), partially diffusion-limited (e.g., for high concentrations of particles with γ_i = 0.1) or in a transition regime (for cloud droplets with diameter greater than 20 μm and γ_i = 0.01 or high concentrations of particles with γ_i = 0.01), depending on the diameter and concentrations of the particle/droplet and the values of the reaction probabilities used. The values of the reaction probabilities selected in MADRID are the nominal values listed by *Jacob* [2000]; i.e., 0.2, 1.0 x 10^{-4}, 1.0 x 10^{-3} and 0.1 for HO_2, NO_2, NO_3 and N_2O_5, respectively.

There are several important yet uncertain variables in the calculation of k_i, such as γ_i and A. γ_i has been measured in the laboratory for a number of gases on various condensed phases but its values may differ by several orders of magnitudes for a given species on different types of surfaces. The surface area of particles depends on the particle number concentrations and size distribution, which exhibit high temporal and spatial variabilities. The surface area of cloud/fog droplets depends on the diameters of cloud/fog droplets and the cloud/fog liquid water content, which can be quite different for different types of clouds/fogs. In addition, k_i is a function of ambient temperature and pressure because ν_i is temperature-dependent and D_{gi} is temperature- and pressure-dependent.

The particle size distribution simulated by MADRID is used to calculate the particle surface area. The droplet size distribution in CMAQ is assumed to be lognormal with a fixed geometric standard deviation and a variable diameter. In CMAQ-MADRID, we assumed that cloud or fog droplets are monodisperse. A droplet diameter of 20 μm was used in the base calculation. Note that the heterogeneous rates of diffusion-limited reactions (R1 and R5) are quite sensitive to the droplet diameter, varying by about one order of magnitude as the droplet diameter varies from 5 μm to 20 μm.

3.3. Atmospheric Deposition

3.3.1 Dry deposition

New precursor and condensable organic species were added in CMAQ for the treatment of SOA formation. Condensable gases typically contain multiple functional groups, such as aldehyde, acid and alcohol groups. Without information on the identities of the condensable compounds in the smog chamber experiments of *Odum et al.* [1997] and *Griffin et al.* [1999], deposition velocities of the organic gases are assumed to be analogous to that of higher aldehydes. To simulate the dry deposition of particles, we used the algorithm of *Venkatram and Pleim* [1999]:

$$V_d = \frac{V_s}{1-\exp\left(-(r_a + r_b)V_s\right)} \tag{8}$$

where V_d is the total dry deposition velocity of the particle, V_s is the gravitational settling (sedimentation) velocity, r_a is the aerodynamic resistance in the lower atmosphere and r_b is the resistance in the quasi-laminar layer near the surface. This approach conserves mass because it accounts for the fact that the resistance component depends on a concentration gradient whereas the sedimentation term does not. The particle dry deposition velocity is calculated for each particle size section and the dry deposition flux is calculated accordingly by size section.

3.3.2 Scavenging and wet deposition

Wet deposition is treated similarly in the CMAQ-MADRID cloud module as in the original CMAQ cloud module [*Roselle and Binkowski*, 1999]. If precipitation occurs, the column from the surface to the cloud base is treated as being in equilibrium between the gas

phase and the droplets. The CMU bulk aqueous-phase chemistry module calculates the droplet concentrations of dissolved gaseous species and activated particulate species in the cloud. Below the cloud, the droplet concentrations of the soluble gases are calculated using their Henry's law constants and the particles are assumed to be completely absorbed into the rain droplets. The column-weighted droplet concentrations are then multiplied by the precipitation rate to calculate the wet deposition fluxes.

One modification was made to the treatment of below-cloud scavenging of gases (washout). In the original CMAQ formulation, the solubility of gases into raindrops is calculated using the Henry's law constant. For chemical species that dissociate in aqueous solutions such as acids (e.g., HNO_3, HCl) and bases (e.g., NH_3), the solubility is then underestimated. In CMAQ-MADRID, we take into account the aqueous dissociation reactions by using the effective Henry's law constant.

4. APPLICATION OF CMAQ-MADRID

CMAQ-MADRID was applied to simulate the August 1987 Southern California Air Quality Study (SCAQS) episode in the Los Angeles basin. Figure 1 shows the simulation domain and the locations of 38 O_3 measurement sites and 8 PM sampling sites in the basin. SCAQS provides a comprehensive database needed for model inputs and evaluation. This episode has been used earlier for the evaluation of PM air quality models [see *Seigneur*, 2001] and, therefore, it provides a convenient benchmark. The PM measurements include concentrations of total $PM_{2.5}$ mass, total PM_{10} mass, sodium (Na^+), sulfate (SO_4^{2-}), ammonium (NH_4^+), nitrate (NO_3^-), chloride (Cl^-), elemental carbon (EC, also referred to as black carbon), and organic carbon (OC). A factor of 1.4 was used to convert the measured OC to organic material (OM) for model comparison [*White and Roberts*, 1977]. Although other inorganic

species such as dust, calcium and iron were not explicitly measured, they contribute significantly to the total PM mass concentration. For example, they account for up to 28% and 53% of the measured 24-hr average $PM_{2.5}$ and PM_{10} mass at the 8 PM sampling sites. In our model, the simulated PM species include Na^+, SO_4^{2-}, NH_4^+, NO_3^-, Cl^-, EC and OM. All other species such as crustal materials are lumped together as other inorganic species (OI).

In the SCAQS simulation, the southwest corner of the modeling domain was placed at 33° 18' N latitude and 119° 24' W longitude. The horizontal grid system consists of 63 x 28 grid cells, with a grid resolution of 5 x 5 km^2. 30 layers of the MM5 grid system were mapped to 15 layers of CMAQ-MADRID, with a one to one mapping near the surface. Two base simulations were conducted, one with 2 size sections and the other with 8 size sections in the size range of 0.0215 and 10 μm to represent particle size distribution. The 2 size sections are 0.0215 - 2.15 μm and 2.15-10 μm, and the 8 size sections are 0.0215-0.0464 μm, 0.0464-0.1 μm, 0.1-0.215 μm, 0.215-0.464 μm, 0.464-1 μm, 1-2.15 μm, 2.15-4.64 μm, and 4.64-10 μm. The CBM-IV gas-phase chemical mechanism, the CMU bulk aqueous-phase chemical mechanism, and the MADRID 1 aerosol module were used in the two base simulations and in all sensitivity simulations except for a sensitivity simulation in which MADRID 2 was used to evaluate the sensitivity to different SOA formulations. The heterogeneous reactions of HO_2, NO_2, NO_3, and N_2O_5 on the surface of particles and that of N_2O_5 on cloud droplets were also accounted for in the base and all sensitivity simulations except one sensitivity simulation in which those heterogeneous reactions were turned off. The particle growth and gas/particle mass transfer were simulated with the moving-center scheme and the CMU hybrid approach, respectively, in the base simulations. Additional simulations were conducted with the finite-difference scheme for particle growth and the CIT bulk and a simple bulk equilibrium approaches for gas/particle mass transfer in the sensitivity studies.

4.1 Meteorology

The meteorological fields were simulated using the meteorological Mesoscale Model version 5 (MM5) with four-dimensional data assimilation. This MM5 simulation has been described previously [*Hegarty et al.*, 1998] and used in previous air quality simulations [*Pai et al.*, 2000; *Seigneur et al.*, 2000a, 2000b]. As discussed in these earlier results, the meteorological fields were mispredicted during daytime (particularly on August 28, at inland locations), which led to overestimated vertical mixing. To minimize the impact of such meteorological inputs on the air quality simulations, we added a post-processing step to the MM5 outputs by developing a diagnostic field of spatially- and temporally-varying mixing heights using data available from acoustic sounders at 9 meteorological monitoring locations within the basin. A vertical diffusion coefficient of 1 m^2 s^{-1} was used to represent these mixing heights.

4.2 Emissions

Emissions of gases and particles generally follow *Pai et al.* [2000]. The emissions of NO_x, CO, SO_2, SO_3 and the CBM-IV speciated VOC are based on the 1987 SCAQS emission inventory of *Allen and Wagner* [1992]. Primary organic compounds in CBM-IV include three explicit species: ethene (ETH), formaldehyde (FORM) and isoprene (ISOP) and six lumped species: single carbon bond (i.e., paraffin or PAR), double carbon bonds (i.e., olefins or OLE), 7-carbon ring structures (i.e., toluene or TOL), 8-carbon ring structures (i.e., xylene or XYL), the carbonyl group and adjacent carbon atom in acetaldehyde and higher molecular weight aldehydes (i.e., acetaldehyde or ALD2) and non-reactive carbon atoms (NR). Non-aromatic anthropogenic SOA precursors are added to either paraffins or olefins or both. For example,

long-chain alkanes are added to paraffins and long-chain alkenes are apportioned to both paraffins and olefins. Because of the reported underestimation in motor vehicle VOC emissions and total VOC emissions [e.g., *Harley et al.*, 1997; *Lu et al.*, 1997], the SCAQS motor vehicle VOC emissions were increased by a factor of 2.4 and the total VOC emissions were then increased by a factor of 1.3 to bring the total VOC emissions in the inventory into agreement with the ratio of 8.8 for VOC/NO_x ambient concentrations. The emissions of NH_3 were obtained from *Meng et al.* [1998], which were originally based on the 1982 NH_3 emission inventory of *Cass and Gharib* [1984].

Larger uncertainties exist in the primary PM emissions, particularly in their size distribution. The emissions of $PM_{2.5}$ and $PM_{10-2.5}$ and PM chemical speciation are based on *Meng et al.* [1998], which was originally created by *Lurmann et al.* [1997] based on the California Air Resources Board's original PM emission inventories. The chemical composition of PM emissions includes SO_4^{2-}, Na^+, Cl^-, EC, OM, and OI (e.g., crustal material) in $PM_{2.5}$ and $PM_{10-2.5}$ size ranges. Note that the OM emissions were obtained by adding 40% to the original OC emissions in the CARB's inventories to account for the oxygen and hydrogen associated with the OC and the original zero OM emission fractions for many emission categories were adjusted by reallocating the original EC fractions between EC and OM [*Lurmann et al.*, 1997]. The adjusted OM emissions are still low compared to those in updated inventories [*Eldering and Cass*, 1996; *Kleeman and Cass*, 1998]. Two adjustments were made in this study to the PM chemical speciation used by *Meng et al.* [1998]. First, 71% of total EC emissions were assigned to the sub-2.5 μm size range. This value is based on the observed mean mass ratio of sub-2.5 μm EC ($EC_{2.5}$) to sub-10 μm (EC_{10}) during this SCAQS episode. ($EC_{2.5}$ accounts for 78% and 80% of total EC emissions in *Meng et al.* [1998] and *Jacobson* [1997b], respectively; however, $EC_{2.5}$ concentrations were overpredicted with a bias

of 30-35% in both works). Second, we assumed that sea salt emissions are 32 tons day^{-1} with 10% in the sub-2.5 μm size range. Neither the SCAQMD nor the CARB emission inventory includes sea salt emissions which produce most of the Na^+ and Cl^- mass. *Lurmann et al.* [1997] and *Meng et al.* [1998] assumed a total NaCl emission of 75 tons day^{-1} with 29% in the sub-2.5 μm size range. *Lurmann* et al. [1997] reported a moderate overprediction of Na^+ and Cl^- with bias of 38% and 24%, respectively. The total oceanic area covered in the simulated domain in *Meng et al.* [1998] is roughly two times larger than that in the current domain. We scaled down the emission rate of 75 tons day^{-1} to 52 and 32 tons day^{-1} in two test simulations. Better agreement between simulated and observed NaCl mass was obtained with 32 tons day^{-1}; this value was therefore used in our simulation. For simulations with 8 size sections, PM emissions were assigned to sections according to the default size distribution of CMAQ [*Byun and Ching*, 1999].

4.3 Initial and Boundary Conditions

Initial conditions (IC) and boundary conditions (BC) for gases follow *Pai et al.* [2000]. IC and BC for PM in the fine and coarse size ranges were speciated into SO_4^{2-}, NO_3^-, NH_4^+, Na^+, Cl^-, EC, OM, and OI using their observed concentrations in the two size ranges from San Nicholas Island, a "background" site during SCAQS 1987. For simulations with 8 size sections, the mass distribution of IC and BC for PM species in each section was determined using the default size distribution of CMAQ [*Byun and Ching*, 1999].

4.4 Results and Discussion

All SCAQS simulations were conducted for the period starting at 4:00 PST on August 25 and ending at 4:00 PST on August 29, 1987. The first two days were used as spin-up days to generate IC for August 27. Results are analyzed and presented for August 27 and 28.

4.4.1 Predicted O_3 mixing ratios at SCAQS sampling sites

Figure 2 shows 2-day time series plots of observed and predicted O_3 mixing ratios at 12 monitoring sites selected to represent various parts of the basin. The predicted O_3 mixing ratios from the two base simulations (with 2 and 8 size sections) are very similar, thus only the predictions with 2 size sections are shown. The sites include El Rio (ELRI), Piru (PIRU), Reseda (RESE), and Thousand Oaks (THSO) in the San Fernando Valley in the northwestern basin (Figures 2a, b, c, and d); central and west Los Angeles (CELA and WSLA) in the western urban and suburban areas (Figures 2e and f); Pomona (POMA) and Riverside (RIVR) in the central and eastern downwind inland area (Figures 2g and h); Crestline (CRES) and Hesperia (HESP) in the northern rural and remote areas (Figures 2i and j); and Long Beach (LBCC) and El Toro (TORO) in the mid and southern coastal areas (Figures 2k and l).

The observed peak O_3 mixing ratios in the basin typically occurred in the early-to-mid afternoon between noon and 4 p.m. In the San Fernando Valley, the predicted daytime and peak O_3 mixing ratios agreed well with the observations, but the predicted time of peak O_3 was sometimes off by a couple of hours. At the central and west Los Angeles sites, the predicted daytime and peak O_3 mixing ratios on August 28 and the time of peak O_3 on both days matched very well with observations, but the O_3 mixing ratios on August 27 were overpredicted by 69% and 54% at CELA and WSLA, respectively. In the central and eastern locations downwind, the predicted time of peak O_3 was slightly delayed and the peak and some daytime O_3 mixing ratios were underpredicted at POMA (by 32%) on August 28 and at RIVR

(by 31% and 53%) on both days. In the northern rural and remote areas (CRES and HESP), the observed daytime O_3 mixing ratios were well predicted with a moderate underprediction (by 22%) in the peak O_3 mixing ratio at CRES on August 27. In the mid to southern coastal sites (LBCC and TORO), the predicted time of peak O_3 was slightly off. The peak O_3 mixing ratios were overpredicted moderately at LBCC on August 28 (by 36%) and at TORO on both days (by 33% and 18%) and significantly at LBCC on August 27 (by 110%). Overall, the model simulations reproduce the magnitude and the spatial and temporal variations of O_3 mixing ratios throughout the basin, but tend to overpredict daytime O_3 mixing ratios at a few sites in the western urban areas and in the mid-to-southern coastal areas on August 27 and underpredict the O_3 mixing ratios at inland sites downwind on August 28. The underpredictions inland are due, at least in part, to overpredictions of the vertical mixing and wind speeds by the meteorological model inland on that day. The uncertainty in precursor emissions may also contribute to the underpredictions. The model also significantly overpredicts the O_3 mixing ratios at night at all sites except El Rio, Long Beach, El Toro, and Hesperia, which is due in part to an underestimation of NO mixing ratios, as a result of an overestimation of vertical mixing in the surface layer, and in part to a relatively high ceiling of the first model layer (i.e., 60 *m*) used.

4.4.2 Predicted PM chemical composition and size distribution

Figures 3 to 6 show the observed and simulated 24-hr average concentrations for $PM_{2.5}$, PM_{10} and their chemical compositions on August 27 and 28 at four sites: Hawthorne (HAWT), Los Angeles (CELA), Azusa (AZUS), and Riverside (RIVR). They represent an upwind coastal site in the western basin, a downtown area with high motor vehicle emissions, a mid-

basin rural/suburban site, and a downwind urban site in the eastern basin, respectively. The model predictions with both two and eight size sections are compared to the observations.

The observed concentrations at the four sites show the evolution of $PM_{2.5}$ and PM_{10} across the basin from the coast to the east. The observed PM concentrations were relatively low near the coast but became significantly higher as the air mass was transported across the basin. PM reached its highest level among all monitoring sites at RIVR on both days. The observed sub-2.5 μm and sub-10 μm sulfate ($sulfate_{2.5}$ and $sulfate_{10}$) concentrations ranged across the basin from 5.7 to 10 μg m^{-3} and 6.8 to 12 μg m^{-3}, respectively. The observed sub-2.5 μm and sub-10 μm nitrate ($nitrate_{2.5}$ and $nitrate_{10}$) concentrations were relatively low near the coast, but increased significantly downwind of the NH_3 source areas in the eastern part of the basin, and the highest ammonium and nitrate concentrations occurred at RIVR. EC and OM concentrations were relatively low near the coast, but increased significantly in the downtown source area and in the northern and eastern basin. AZUS had the highest $EC_{2.5}$ and OM_{10} concentrations on both days, the highest EC_{10} on August 27, and the highest $OM_{2.5}$ on August 28. The highest EC_{10} occurred at RIVR on August 28. The highest $OM_{2.5}$ occurred at CLAR on August 27 (not shown), a northern site close to AZUS ($OM_{2.5}$ at AZUS was the second highest across the basin). Compared to other PM compositions, the observed sub-2.5 μm and sub-10 μm sodium ($sodium_{2.5}$ and $sodium_{10}$) and chloride ($chloride_{2.5}$ and $chloride_{10}$) concentrations were relatively low, with a range of 0.04-0.34, 1.28-2.31, 0.04-0.4 and 0.31-1.08 μg m^{-3} at all 8 sites, respectively. Note that most measured $chloride_{2.5}$ and some measured $chloride_{10}$ concentrations were below the detection limit of 0.5 μg m^{-3} for Teflon filters [*Fraser et al.*, 1996].

Similar to O_3 predictions, the model tends to overpredict PM concentrations at coastal and western sites on August 27 but underpredict PM concentrations at inland sites downwind

on August 28. This can be partially attributed to the overpredictions on August 27 and the underpredictions on August 28 in the concentrations of precursors for secondary PM as a result of mispredicted wind speeds and vertical mixing. Other factors that are responsible for the discrepancies between observations and predictions are discussed later along with model performance evaluation. Although some discrepancies exist in the magnitudes of observed and simulated PM and its composition at some locations, the simulations with both size resolutions reproduce well the observed evolution of PM and its composition. The predicted sulfate concentrations from the two base simulations match well with the observed values at all sites except at HAWT, where there was a significant overprediction (by 67% for $sulfate_{2.5}$ and 51% for $sulfate_{10}$) on August 27 and underprediction (by 51% for $sulfate_{2.5}$ and 54% for $sulfate_{10}$) on August 28, and at CELA, where there was a significant overprediction (by 74% for $sulfate_{2.5}$ and 55% for $sulfate_{10}$) on August 27.

The predicted ammonium and nitrate concentrations from both simulations are lower near the coast and higher at downwind locations, with the highest nitrate concentrations occurring at RIVR on both days. The highest $nitrate_{2.5}$ concentrations predicted at RIVR are 28.9 and 18.3 $\mu g\ m^{-3}$ with 2 size sections and 29.8 and 18.8 $\mu g\ m^{-3}$ with 8 size sections on August 27 and 28. For comparison, the observed $nitrate_{2.5}$ concentration at RIVR were 33.3 and 39.8 $\mu g\ m^{-3}$ on August 27 and 28, respectively. The nitrate concentrations predicted with 2 size sections agree well with the observations at CELA and RIVR on August 27 (with a deviation of 8-18%), but show moderate to significant underpredictions (by 32-88%) on August 28 and at other sites on both days. The nitrate concentrations predicted with 8 size sections are similar to those with 2 size sections except that there is a moderate overprediction (by 41-42% for $nitrate_{2.5}$ and 47-52% for $nitrate_{10}$) at HAWT and CELA on August 27. The predicted $nitrate_{2.5}$ and $nitrate_{10}$ concentrations with 8 size sections are 5.3 and 6.8 $\mu g\ m^{-3}$ at

HAWT and 12 and 13.9 μg m^{-3} at CELA. For comparison, the observed values were 3.7 and 4.5 μg m^{-3} at HAWT and 8.5 and 9.5 μg m^{-3} at CELA, respectively. Such an overprediction seems large in terms of percentage but less significant in terms of the absolute values. Moreover, the observed $nitrate_{10}$ concentrations are likely underestimated due to mass losses on the Teflon filter [*Hering et al.*, 1997]. The sensitivity of the predicted nitrate concentrations to size resolution has been studied in *Koo et al.* [2003]. They found that lower nitrate concentrations are predicted by the CMU hybrid approach when a lower size resolution is used, which is consistent with our results. This sensitivity is primarily caused by the mixing of aerosol populations with different composition (e.g., the larger alkaline particles are mixed with the smaller acidic particles in coastal areas) that usually results in an underprediction of the nitrate concentrations when a lower size resolution is used [Capaldo et al., 2000]. For a higher size resolution, more nitrate can be formed in the fine particle size range due to the "bulk equilibrium treatment" and the weighting scheme that is based on surface area, which assigns more condensates to smaller size sections [*Koo et al.*, 2003]. Differences in the removal efficiency and the second order thermodynamic effects that are size-dependent (thus size resolution-dependent) may also contribute to the predicted sensitivity. Compared to nitrate predictions, better agreement is obtained between the simulated (with both size resolutions) and observed ammonium concentrations at all sites.

EC concentrations are underpredicted by 41-67% with both size resolutions at almost all sites on both days, due mainly to uncertainties in meteorological inputs, EC emissions and the size distribution of emitted EC. The OM concentrations are also underpredicted moderately on August 28 in the western downtown area (e.g., by 37-38% for $OM_{2.5}$ at CELA) and significantly near the coast (e.g., by 59-60% for $OM_{2.5}$ at HAWT), in some areas in the northern basin (e.g., by 57-58% for $OM_{2.5}$ at AZUS but not at CLAR) and downwind in the

eastern basin (e.g., by 68-69% for $OM_{2.5}$ at RIVR). The OM predictions on August 27 show a better agreement with observations at all sites (e.g., underpredictions by 18-22%, 12-17%, 37-39% and 52-53% for $OM_{2.5}$ at CELA, HAWT, AZUS and RIVR, respectively). The predicted $sodium_{2.5}$ and $chloride_{2.5}$ concentrations in the two base simulations are in the range of 0.04-0.13 and 0.01-0.31 μg m^{-3} at the four sites, which are generally within the observed range (0.04-0.34 and 0.06-0.4 μg m^{-3}, respectively). The predicted $sodium_{10}$ and $chloride_{10}$ concentrations are in the range of 0.7-1.16 and 0.11-0.82 μg m^{-3} at these sites. At most of these sites, the model tends to underpredict the observed $sodium_{10}$ and $chloride_{10}$ concentrations (1.28-2.31 and 0.31-1.08 μg m^{-3}, respectively) by 36-58% and 20-90%.

Particle size distributions of individual inorganic ions and organic species were measured with the electrical aerosol analyzer (EAA), the laser optical particle counter (OPC), the 9-stage Berner impactors (BI, for inorganic ions) and the micro-orifice uniform deposit impactor (MOUDI, for organic ions) in 11 summer time intensive sampling days at Claremont and Riverside during 1987 SCAQS [e.g., *John et al.*, 1990; *Hering et al.*, 1997]. The measured particle aerodynamic diameter range is 0.03-0.3 μm for EAA, 0.1-3 μm for OPC, 0.075-16.5 μm for BI and 0.1-3 μm for MOUDI [*Hering et al.*, 1997]. *Hering et al.* [1997] obtained a representative particle mass distribution over the size range of 0.03 to 3 μm, measured by EAA, OPC and impactors (BI and MOUDI), for Claremont and Riverside by averaging all summer samplings to compare PM measurements with different techniques and to study the characteristics of PM mass size distribution in the southern California. The observed representative PM mass distributions summed those of individual PM species including SO_4^{2-}, NO_3^-, NH_4^+, EC and OM (=1.4 x measured OC). Figure 7 compares the predicted PM mass size distribution for the above five PM components on August 28, 1987 with the impactor average PM mass size distribution obtained by *Hering et al.* [1997] at Claremont and

Riverside. We discuss here the base 8-section simulation results obtained with the moving-center scheme and the CMU hybrid approach. Results with other combinations of algorithms for particle growth and gas/particle mass transfer are also shown in Figure 7 but will be discussed later in the sensitivity study.

The model correctly predicts a unimodal distribution for accumulation mode PM that is typical at Riverside during the summer time but it fails to reproduce the typical bimodal distribution of accumulation mode PM at Claremont (A bimodal distribution was however, predicted for some time periods at Claremont and in other locations, see section 4.5.3). The predicted peak value at Riverside is higher than that at Claremont and both peak values occur in the same size range, consistent with observations. However, the PM mass concentration peaks in the size section of 0.215-0.464 μm at both sites, which is somewhat off from the diameter of the observed peak values (i.e., 0.52 μm). The peak values are underpredicted by 30% at Claremont and 16% at Riverside. In addition to the aforementioned factors (e.g., mispredictions in meteorology and uncertainties in emissions of primary PM species and precursors of secondary PM species) that contribute to differences between observed and simulated PM mass and composition, the discrepancy in observed and predicted particle size distribution indicate that a finer size resolution (> 8 sections) is needed to accurately simulate PM size distribution.

4.4.3 Model performance evaluation

The model performance is evaluated following the guidance developed by *Seigneur et al.* [2000c]. Our evaluation focuses on the mean normalized gross error (MNGE) and mean normalized bias (MNB) in the O_3 and PM predictions at the sampling sites. Table 2 shows the MNGE and MNB for 1-hr average O_3 mixing ratios and 24-hr average concentrations of $PM_{2.5}$,

PM_{10} and their components averaged over all sampling sites on August 27 and 28, 1987. Table 2 also shows the ranges of MNGE and MNB obtained from simulations of SCAQS episodes with other 3-D air quality models including GATOR [*Jacobson*, 1997b], CIT [*Harley et al.*, 1993, 1997; *Meng et al.*, 1998], and UAM-AERO [*Lurmann et al.*, 1997]. GATOR and CIT were applied to the same episode whereas UAM-AERO was applied to a June 1987 episode. Only statistics obtained from the CMAQ-MADRID simulation with 2 sections are presented in Table 2. In the following analysis and discussion, we focus on results from the simulation with 2 size sections. The statistics obtained from the simulation with 8 sections are somewhat different from those with 2 sections. The differences between the results in the two base simulations will be discussed in the relevant sections below.

The MNGE and MNB in O_3 predictions with both size resolutions at 38 sites are 36% and 20% for August 27 and 31% and -3% for August 28. The statistical values were calculated for each day using a cut off value of 40 ppb for O_3. The MNGE and MNB are within the range of other work (e.g., *Jacobson* [1997b], *Meng et al.* [1998], and *Lurmann et al.* [1997]).

The performance statistics for $PM_{2.5}$, PM_{10} and their components were calculated at 8 PM sampling sites in the modeling domain. The predicted mean $PM_{2.5}$ and PM_{10} mass concentrations averaged over all 8 locations are 51.8 and 91.7 $\mu g\ m^{-3}$ on August 27, which overpredict the mean observed values of 42.3 and 75.9 $\mu g\ m^{-3}$ by 21-22%. The predicted mean $PM_{2.5}$ and PM_{10} concentrations averaged over all 8 locations are 43.4 and 81.3 $\mu g\ m^{-3}$ on August 28, which compare well with the observed values of 48.1 and 85.3 $\mu g\ m^{-3}$. The MNGE and MNB in the predicted $PM_{2.5}$ concentrations are 42% and 30% on August 27 and 47% and -2% on August 28. The MNGE and MNB in PM_{10} concentrations are slightly higher (53% and 33% for August 27 and 56% and 8% for August 28). For the simulation with 8 size sections, the MNGE and MNB in the predicted $PM_{2.5}$ concentrations are very similar to those with 2 size

sections on August 28 but slightly higher on August 27 (45% and 32%, respectively). These performance statistics for both $PM_{2.5}$ and PM_{10} mass concentrations are consistent with those obtained with the other three models.

The predicted $sulfate_{2.5}$ and $sulfate_{10}$ concentrations match the observations well at all sites, with MNGE and MNB of 27% to 49% and -27% to 49% for $PM_{2.5}$ sulfate and 35% and -35% to 32% for PM_{10} sulfate. The MNGE and MNB are lower with 8 size sections for $PM_{2.5}$ and PM_{10} sulfate (40% and 38% for $PM_{2.5}$ sulfate and 31% and 25% for PM_{10} sulfate) on August 27 but slightly greater (30% and -30% on for $PM_{2.5}$ sulfate and 37% and -37% for PM_{10} sulfate) on August 28. These values are commensurate with those obtained in other SCAQS simulations. The predicted mean $sulfate_{2.5}$ and $sulfate_{10}$ concentrations are 9.5 and 10.2 $\mu g\ m^{-3}$ on August 27 and 6.3 and 6.8 $\mu g\ m^{-3}$ on August 28. The corresponding observed values are 6.5 and 7.9 $\mu g\ m^{-3}$ on August 27 and 8.8 and 10.6 $\mu g\ m^{-3}$ on August 28. In addition to direct emissions within the basin, particulate sulfate concentrations are also affected by the upwind boundary conditions and the formation of H_2SO_4 via SO_2 oxidation. Large uncertainties exist in the particulate sulfate emissions and the upwind sulfate boundary concentrations, which may contribute to the moderate overprediction on August 27 and underprediction on August 28 in both $sulfate_{2.5}$ and $sulfate_{10}$. Upwind boundary concentrations of 2.1 and 2.6 $\mu g\ m^{-3}$ were used for $sulfate_{2.5}$ and $sulfate_{10}$, respectively The prevailing surface wind for this episode was westerly and blew from the western coast to the inland mountains throughout the basin [*Lu et al.*, 1997]. The 8 PM sites are either located near the coast (e.g., HAWT) or inland along the trajectory of the prevailing wind, the upwind boundary conditions were found to contribute significantly (up to 35% contribution) to sulfate formation at those sites. The oxidation of SO_2 is slow in the absence of clouds but the gas-phase SO_2 oxidation produces up to 1.0 - 1.5 ppb (4 - 6 $\mu g\ m^{-3}$) of H_2SO_4 at the 8 PM sampling sites, which may contribute up to 75% and 33%

of hourly and 24-hr average concentrations of sulfate$_{2.5}$, respectively, for this episode. The moderate overprediction on August 27 and underprediction on August 28 in particulate sulfate concentrations may, therefore, also result from the gas-phase formation of H_2SO_4 via SO_2 oxidation by OH radicals. OH is primarily produced through the photolytic reaction of O_3 and subsequent hydrolysis reaction of $O(^1D)$ with H_2O. The predicted O_3 and water vapor concentrations on August 28 are lower than those on August 27 at most sites in the northern and eastern portions of the SCAQS domain (e.g., BURK, CELA, RIVR), resulting in relatively high total gas-phase oxidizing capacity (i.e., higher OH levels) on August 27 and relatively lower oxidizing capacity (i.e., lower OH levels) on August 28. At coastal sites (e.g., HAWT and LBCC) and one northern site (i.e., AZUS), the OH levels on August 28 are similar to those on August 27, but the predicted SO_2 mixing ratios are lower than those on August 27 due possibly to some biases in other predicted meteorological variables such as wind fields that affect diffusion and transport of species. This could also contribute to lower H_2SO_4 formation on August 28 at those sites.

Two techniques were used to measure particulate nitrate during SCAQS. The Teflon filter method was used to measure both nitrate$_{2.5}$ and nitrate$_{10}$, and the denuder difference method was used to measure nitrate$_{2.5}$ only. Large discrepancies were found between the observed nitrate$_{2.5}$ concentrations obtained with these two techniques, and the denuder difference method is believed to be more accurate than the Teflon filter method [*Hering et al.*, 1997]. The observed nitrate$_{10}$ concentrations obtained with the Teflon filter were sometimes even lower than the nitrate$_{2.5}$ concentrations measured with the denuder difference method, suggesting that the Teflon filter method may underestimate nitrate$_{10}$ mass. Therefore, the nitrate$_{2.5}$ measurements obtained with the denuder difference method were used here. The predicted mean nitrate$_{2.5}$ and nitrate$_{10}$ concentrations are 10 and 11.6 $\mu g\ m^{-3}$, respectively, on

August 27 and 7.5 and 8.4 μg m^{-3} on August 28. The corresponding observed values are 13.2 and 12.1 μg m^{-3} on August 27 and 16.6 and 13.5 μg m^{-3} on August 28. The MNGE and MNB in predicted $nitrate_{2.5}$ concentrations are 29% and -25% on August 27 and 60% and -51% on August 28. The corresponding values in predicted $nitrate_{10}$ concentrations are 25% and -1% on August 27 and 59% and -27% on August 28. While the model tends to overpredict nitrate mass at night, it underpredicts nitrate mass during the day, resulting in an underprediction in 24-hr average $nitrate_{2.5}$ concentrations on both days and in $nitrate_{10}$ concentrations on August 28. For the simulation with 8 size sections, $nitrate_{2.5}$ concentrations are somewhat overpredicted (instead of underpredicted) at HAWT and LBCC on August 27 (e.g., see Figure 3), resulting in a net overprediction, with MNGE and MNB of 44% and 10% for $nitrate_{2.5}$ and 47% and 27% for $nitrate_{10}$ on August 27. The statistics on August 28 with 8 size sections are slightly improved for $nitrate_{2.5}$ with MNGE and MNB of 58% and -47% but slightly worse for $nitrate_{10}$ with MNGE and MNB of 62% and -29%.

The particulate nitrate can be formed through dissolution or condensation of HNO_3 on the surface of particles and the heterogeneous reactions of nitrogen species such as N_2O_5 and NO_3 on the surface of wet particles. Ammonium nitrate (NH_4NO_3) and sodium nitrate ($NaNO_3$) are the most common nitrate salts. The formation of particulate nitrate can be limited by the abundance of HNO_3 (i.e., NO_x-limited), NH_3 (i.e., NH_3-limited) or ambient water vapor (i.e., H_2O-limited), depending on the chemical and meteorological conditions at a specific location. Therefore, the accuracy in nitrate predictions depends not only on the accuracy of meteorology and emissions of precursors (e.g., NO_x and NH_3) but also on the accuracy of the gas- and aqueous-phase chemistry as well as gas-to-particle conversion processes simulated.

Few clouds were present during this SCAQS episode; therefore, HNO_3 formation was governed primarily by gas-phase reactions and to a lesser extent heterogeneous reactions. Gas-

to-particle conversion was simulated with the CMU hybrid approach in the base simulations, in which ISORROPIA is used to calculate the particulate-phase concentrations. ISORROPIA has been shown to produce better fine NH_4^+ and NO_3^- predictions than SEQUILIB [*Nenes et al.*, 1999] (SEQUILIB was used in the simulations of SCAQS June 24-26 episode of *Lurmann et al.*, 1997). In addition, we tested the performance of ISORROPIA under 400 cases typical of the atmospheric conditions in the eastern and the western U.S. and found that the predictions of total PM and its chemical composition by ISORROPIA are comparable with those predicted by the more comprehensive equilibrium modules such as SCAPE2 and EQUISOLV II. The underpredictions in the NO_3^- concentrations are, therefore, unlikely related to the model treatment of thermodynamic equilibrium in MADRID. Other work has also shown that given the correct total concentrations, the PM nitrate can be reproduced reasonably well by ISORROPIA, considering the measurement error and the bulk equilibrium assumption [*Nenes et al.*, 1999; *Ansari and Pandis*, 1999].

The formation of nitrate was unlikely NO_x-limited since there were generally abundant HNO_3 on both days at many locations. Underpredictions in NH_3 mixing ratios may contribute to the underpredictions of NO_3^- concentrations at some western and central sites such as HAWT and ANAH on August 28 when the formation of NH_4NO_3 was NH_3-limited. The predicted low NH_3 mixing ratios during daytime may also contribute to low NO_3^- formation at other inland locations, especially in the eastern domain. For example, the observed 24-hr average NH_3 mixing ratio for August 28 was 1.4 ppb at HAWT and 15.1 ppb at RIVR. For comparison, the predicted 24-hr average NH_3 mixing ratio for the same day was 0.7 ppb at HAWT and 8.8 ppb at RIVR. Underestimation of the ambient RH during daytime is likely another factor that contributed to the underprediction of NO_3^-. For example, the observed daytime RH values during August 27-28 range from 65-83% at HAWT and 28-60% at RIVR,

while the predicted daytime RH values range from 44-75% at HAWT and 16-45% at RIVR. Therefore, the predicted low RH limited to some extent the dissolution and condensation of HNO_3, resulting in lower NO_3^- formation during daytime on both days.

The biases in predicted meteorological fields may also have affected NH_4^+ predictions that depend on the accuracy of the precursor emissions and the predicted meteorological conditions. The predicted mean sub-2.5 μm and sub-10 μm ammonium (ammonium$_{2.5}$ and ammonium$_{10}$) concentrations are 6.2 and 6.3 μg m^{-3} on August 27, which are higher by 51% and 40% than the observed values of 4.1 and 4.5 μg m^{-3}. The predicted mean ammonium$_{2.5}$ and ammonium$_{10}$ concentrations are 4.6 and 4.7 μg m^{-3} on August 28, which are lower by 18% and 19% than the observed values of 5.6 and 6.1 μg m^{-3}. The MNGE and MNB at all 8 sites are 61% on August 27 and 44% and -11% on August 28 for predicted ammonium$_{2.5}$ concentrations and 50% and 47% on August 27 and 44% and -19% on August 28 for predicted ammonium$_{10}$ concentrations. The NH_3 emission inventory used here was based on 1982 NH_3 emissions estimated by *Cass and Gharib* [1984]; therefore, it may not accurately reflect the actual total NH_3 emissions and their regional distributions in 1987. Also, since the sulfate$_{2.5}$ concentrations are dominated by $(NH_4)_2SO_4$, the moderate overprediction on August 27 and underprediction on August 28 in SO_4^{2-} and NH_4^+ are highly correlated. The underprediction in NH_4^+ on August 28 also correlates with the underprediction in NO_3^-, since nitrate$_{2.5}$ concentrations are dominated by NH_4NO_3 in the particulate phase. The overpredictions on August 27 and underpredictions on August 28 in NH_4^+ concentrations are most likely caused by biases in the predicted meteorological variables such as wind fields.

The predicted mean $EC_{2.5}$ and EC_{10} mass are, respectively, 1.8 and 2.3 μg m^{-3} on August 27 and 1.7 and 2.2 μg m^{-3} on August 28. These values are lower than the observed values of 2.5 and 3.3 μg m^{-3} on August 27 and 2.8 and 4.0 μg m^{-3} on August 28. The statistics

obtained with both 2 and 8 size sections are quite similar. As discussed above, large uncertainties exist in the PM emission inventories that affect the predicted EC concentrations.

The predicted mean $OM_{2.5}$ concentrations are 7.3 and 6.8 μg m^{-3} on August 27 and 28; these values are lower by 22% and 40% than the observed values of 9.4 and 11.4 μg m^{-3}. The predicted OM_{10} concentrations are 13.9 and 13.0 μg m^{-3} on August 27 and 28; the corresponding observed values are 13.6 and 16.9 μg m^{-3}. The MNGE and MNB at all 8 sites are 38% and -14% on August 27 and 61% and -28% on August 28 for $OM_{2.5}$ concentrations and 54% and 17% on August 27 and 65% and -7% on August 28 for OM_{10} concentrations. The simulation with 8 size sections predicted similar MNGE and MNB, with 40% and -17% on August 27 and 61% and -29% on August 28 for $OM_{2.5}$ concentrations and 53% and 14% on August 27 and 65% and -8% on August 28 for OM_{10} concentrations. Those values are generally consistent with those obtained in earlier SCAQS simulations; except for slightly higher MNGE for $OM_{2.5}$ and OM_{10} predictions on August 28 and a slightly higher MNB for OM_{10} predictions on August 27.

The observed OM comprises both primary and secondary organics, but the ambient monitoring data do not separate them. A direct evaluation of SOA predictions is thus not possible. The underpredictions in $OM_{2.5}$ concentrations are likely due to underestimates in both the primary OC emissions and SOA formation. The SOA percentages in OM_{10} predicted in the base simulations with MADRID 1 range from 1.7% to 10.9% at the sampling sites; these values are significantly lower than the estimated values of 10-75% for the SCAQS domain [*Pandis et al.*, 1993], particularly on August 28. In addition to the overpredicted wind speeds and vertical mixing that led to an underestimation of VOC precursor mixing ratios of SOA, several factors may contribute to this underestimate. First, large uncertainties exist in the emissions of SOA precursor VOC species in the SCAQS inventory as discussed previously.

Different adjustments have been applied to the original CARB emission inventories for SCAQS 1987 in various modeling studies, resulting in quite different VOC emissions used in these studies. For example, the adjusted daily emissions of TOL and XYL used in *Jacobson et al.* [1996], *Lu et al.* [1997], *Meng et al.* [1998] and this work are 239 and 201 tons, 378 and 301 tons, 214 and 174 tons, and 314 and 226 tons, respectively. Most previous gas-phase simulations [e.g., *Jacobson et al.*, 1996; *Harley et al.*, 1993; 1997] and this work underpredicted O_3, whereas *Lu et al.* [1997] predicted O_3 mixing ratios in excellent agreement with observations. This implies that the VOC precursor emissions used in all these work except *Lu et al.* [1997] may be somewhat underestimated. Emissions of other anthropogenic SOA precursors such as long-chain alkanes and alkenes, cresols and phenols have little impact on the predicted SOA in MADRID 1 because (1) those species are not considered as SOA precursors in MADRID 1, (2) they are represented by separate mechanism species in CBM-IV, thus not included in TOL and XYL. Second, uncertainties may also exist in the partition coefficients that were obtained at experimental temperatures of 301 K to 316 K and were corrected for temperature dependence at other ambient temperatures. The SOA formation is highly sensitive to the selection of the enthalpy of vaporization in Equation 2 that was used to account for the temperature dependence. Although the temperature dependence of the partition coefficients was taken into account, the partition coefficients used in MADRID 1 are roughly lower by a factor of 2 than those calculated with the formulation of *Pankow* [1994] in MADRID 2. Third, the SOA module in MADRID 1 only includes two anthropogenic surrogate aromatic precursors, namely, TOL and XYL, while other anthropogenic VOC (e.g., long-chain alkanes and alkenes, cresol and phenols) may yield to SOA formation. *Pandis et al.* [1992] simulated SOA formation for the same SCAQS episode and found that the CBM-IV surrogate aromatic species (i.e., toluene, xylenes and alkylbenzens) contributed to at most 55%

of SOA formation. Biogenic SOA formation was found to be negligible in our simulation in the SCAQS domain due to low biogenic emissions. This is consistent with the low biogenic SOA formation in another Los Angeles basin simulation [*Griffin et al.*, 2002]. Considering additional VOC precursors of SOA will reduce the SOA (thus OM) underpredictions. A sensitivity simulation was thus conducted with a more detailed SOA module (i.e., MADRID 2), which includes 42 anthropogenic condensable VOC precursor species (see section 4.5.2).

Since the measured fine chloride concentrations were below the detection limit and highly uncertain, we thus focus our evaluation on $sodium_{10}$ and $chloride_{10}$. The predicted $sodium_{10}$ concentrations agree well with observations at all sites, with MNGE and MNB of 37 to 39% and -35 to -34%, respectively, whereas the statistics deteriorate somewhat for the predicted $chloride_{10}$ mass with MNGE and MNB of 49 to 80% and -34 to 3%, respectively. The MNGE and MNB predicted with 8 size sections are slightly worse for $sodium_{10}$ (40 to 49% and -41 to -38%, respectively), and significantly worse for $chloride_{10}$ (63 to 101% and 8 to 49%, respectively), which exemplifies the difficulty in simulating the volatility of HCl for multiple size sections. The predicted mean $sodium_{10}$ and $chloride_{10}$ concentrations are 1.1 and 0.5 $\mu g\ m^{-3}$ on August 27 and 1.1 and 0.73 $\mu g\ m^{-3}$ on August 28. The corresponding observed values are 1.7 and 0.76 $\mu g\ m^{-3}$ on August 27 and 1.7 and 0.72 $\mu g\ m^{-3}$ on August 28. The large MNGE in the predicted $chloride_{10}$ on August 28 resulted from a significant overprediction in terms of percentage in $chloride_{10}$ concentration at Anaheim (ANAH) and Long Beach (LBCC) (1.8 and 1.2 $\mu g\ m^{-3}$, respectively), where a low 24-hr average $chloride_{10}$ concentration of 0.5 $\mu g\ m^{-3}$ was observed. The discrepancy between observed and simulated Cl^- concentrations may be attributed to several major factors including the uncertain sea salt emissions used, the mispredicted wind speeds and vertical mixing, and the simplified thermodynamic treatment involving chlorine species used. The observed 24-hr average $chloride_{10}$ concentrations at

coastal sites such as ANAH and LBCC were lower than those at other inland sites (0.75-0.86 $\mu g\ m^{-3}$). This can be explained by the changes in the dominant reactions involving Cl^- and HCl as air parcels travel from coast to inland areas. The following equilibria control the abundance of Cl^-:

$$NaCl_{(s)} + HNO_{3(g)} \leftrightarrow HCl_{(g)} + NaNO_{3(s)} \quad (R6)$$

$$NH_4Cl_{(s)} + HNO_{3(g)} \leftrightarrow HCl_{(g)} + NH_4NO_{3(s)} \quad (R7)$$

$$NaCl_{(s)} \leftrightarrow Na^+_{(aq)} + Cl^-_{(aq)} \quad (R8)$$

$$H^+_{(aq)} + Cl^-_{(aq)} \leftrightarrow HCl_{(g)} \quad (R9)$$

$$HCl_{(g)} + NH_3(g) \leftrightarrow NH_4Cl_{(s)} \quad (R10)$$

R6-R9 are dominant near the coast (where little NH_3 available), moving Cl^- to the gas phase as HCl and leading to a lower Cl^- concentration. R10 becomes dominant over inland areas due to the availability of NH_3, resulting in an increased Cl^- concentration in the particulate phase as NH_4Cl(s). R6 and R8-R10 also contribute to the repartitioning of Cl^- from coarse to fine size sections, which is supported by the fact that a significant fraction of Cl^- was observed in the submicrometer particles in Claremont during this episode [*Wall et al.*, 1988]. In the CMU hybrid approach, the thermodynamic equilibrium for fine particles is treated with ISORROPIA, which includes R8-R10 but not R6 and R7 (R6 and R7 may be important when RH < 60%). For coarse particles, MADM is used, which includes R6 and R8-10 but R6 is solved only for dry particles (typically when RH < 40%). The observed daytime RH at most coastal or near coastal sites ranged from 40% to 60%, implying that neglecting R6 and R7 may possibly contribute to the discrepancy between observed and simulated Cl^- for this episode. While our model predicts some fine Cl^- through R8-R10 under high RH conditions (i.e., at night or in the morning), a more comprehensive thermodynamic module that includes all important gas-solid

equilibria involving chlorine species may be needed to reproduce the variation trends in the Cl^- as air parcels travel from coast to inland areas. Nevertheless, the existing thermodynamic module in MADRID is suitable for most applications, considering the uncertainty in the chloride measurements and the difficulty in simulating volatile chlorine species.

4.5 Sensitivity Analyses

Sensitivity studies to uncertainties in VOC and NO_x emissions in the SCAQS inventory have been previously performed by many investigators [e.g., *Pandis et al.*, 1992; *Lu et al.*, 1997; *Harley et al.*, 1997]. We focus here on the sensitivity of model predictions to several unique treatments and formulations in CMAQ-MADRID including heterogeneous reactions of HO_2, NO_2, NO_3 and N_2O_5 on the surface of particles and droplets; two SOA modules that treat different numbers of condensable VOC precursor species with different partitioning mechanisms; two numerical schemes for simulating particle growth by condensation [or shrinkage by volatilization]; and three approaches for simulating gas/particle mass transfer. As shown below, these treatments/formulations can be major sources of uncertainties in 3-D O_3 and PM modeling.

4.5.1 Sensitivity to heterogeneous reactions

Figure 8 shows the predicted gas-phase mixing ratios of HO_2, H_2O_2, HNO_3 and O_3 at a coastal site (HAWT) with and without heterogeneous reactions. The heterogeneous reactions provided a source for H_2O_2 and HNO_3 throughout the simulation period, a sink for HO_2 during all the period except in the morning. The O_3 mixing ratios at HAWT decreased slightly (< 4%) throughout the simulation period except between the sunrise and noon when there was an appreciable 0.3-7.8 ppb increase (by 0.4-16.7%). At this coastal site, the reactions that contribute to O_3 production include $O(^1D)+H_2O$, $NO_2+h\nu$, and CO+OH, CH_4+OH, and

HO_2+NO. The reactions that contribute directly or indirectly to O_3 destruction include $O(^1D) \rightarrow O(^3P)$, OH+$NO_2$, O_3+NO, C_2O_3+NO_2, HO_2+HO_2+H_2O and HO_2+HO_2. The heterogeneous reaction of NO_2 continued to be an important sink for NO_2 in the morning, resulting in lower NO_2 (by 4-7%) and lower NO (by 6-19%) mixing ratios. While a lower NO_2 mixing ratio can lead to a lower O_3 in the morning, a lower NO and higher OH and HO_2 mixing ratios can lead to a higher O_3 mixing ratio by reducing the consumption rate of O_3 by NO and increasing the oxidation rate of CO and CH_4 by OH and that of NO by HO_2. The latter effect dominated in the morning, resulting in a net increase in O_3 mixing ratios at HAWT.

The changes in the gas-phase species due to heterogeneous reactions caused corresponding changes in $PM_{2.5}$, PM_{10} and their components such as SO_4^{2-} and NO_3^- at HAWT, as shown in Figure 9. The 24-hr average $sulfate_{2.5}$ and $sulfate_{10}$ concentrations with heterogeneous reactions were higher by 0.55 and 0.68 μg m^{-3} (by 6.7 and 7.5%, respectively) than those without heterogeneous reactions on August 27 at HAWT. This resulted from a higher aqueous-phase oxidation of SO_2 by H_2O_2 in cloud droplets between 1-6 a.m. and a higher gas-phase oxidation of SO_2 by OH between sunrise and noon. The changes in the 24-hr average $nitrate_{2.5}$ and $nitrate_{10}$ concentrations at HAWT were opposite those of SO_4^{2-}, namely, 1.25 and 1.21 μg m^{-3} (by 19.1 and 15.1%, respectively) lower on August 27. The heterogeneous reactions of NO_2, NO_3 and N_2O_5 can either increase or decrease NO_3^- formation, depending on the physical and chemical conditions. These reactions may produce more HNO_3 that remain primarily in the gas-phase in the absence of NH_3 and would then condense on particles to form NH_4NO_3 due to the availability of NH_3. On the other hand, NO_3^- formation may be reduced in the presence of these heterogeneous reactions due to a lower gas-phase oxidation of NO_2 by OH (due to lower NO_2 and OH at night), a lower aqueous-phase formation rate (due to lower dissolved NO_2 and NO_3 radicals) between 1 a.m. and 6 a.m. and a lower

oxidation of NO_2 by OH (due to lower NO_2) between sunrise and noon. The latter effect dominated, resulting in lower 24-hr average NO_3^- concentrations on August 27. As a net result of a higher SO_4^{2-} and a lower NO_3^- on August 27, the 24-hr average $PM_{2.5}$ and PM_{10} mass concentrations were lower by 0.77 and 0.47 μg m^{-3}, respectively, on August 27.

The effect of heterogeneous reactions on hourly concentrations of $PM_{2.5}$, PM_{10} and their components is more significant than that for their 24-hr average concentrations. For example, the hourly $nitrate_{10}$ concentrations increased by up to 7.3 μg m^{-3} (~19%) at RIVR and 20 μg m^{-3} (~47%) at ANAH when heterogeneous reactions were included. The changes in the predicted hourly concentrations of $sulfate_{10}$, $ammonium_{10}$ and $nitrate_{10}$ were up to 21%, 25% and a factor of 12, respectively, at the 8 PM sampling sites. Uncertainties are associated with the reaction probabilities of the heterogeneous reactions used in the simulations and with the simulated surface areas of particle and droplets.

4.5.2 Sensitivity to SOA formulations

A simulation was conducted with MADRID 2 of *Pun et al.* [2002], which represents the 42 condensable organic products of the CACM using 10 surrogate compounds: 5 hydrophobic organic compounds that partition into the particulate-phase and 5 surrogate hydrophilic organic compounds that dissolve into an aqueous phase to form SOA. Compared to the SOA formulation in MADRID 1, MADRID 2 treats 28 hydrophobic aromatic SOA precursors and their second- and third-generation products such as benzene-based aromatics with low and high volatility, naphthalene-based and aliphatic compounds. In addition, MADRID 2 treats 14 water-soluble organic compounds and their second- and third-generation products that are dissociative and non-dissociative.

The 24-hr average SOA concentrations predicted with MADRID 2 at the sampling sites increased from 0.06-0.6 to 1.6-6.1 μg m^{-3} (by a factor of 9 to 45). Compared to the results obtained with MADRID 1, the predicted SOA percentages in OM_{10} increased from 2-11% to 15-62%. For example, the 24-hr average SOA concentrations predicted by MADRID 2 at Claremont on August 27 and 28 are 6.1 and 3.2 μg m^{-3}, which are a factor of 10 and 12 higher than those predicted by MADRID 1. With increased SOA formation, the simulation with MADRID 2 improved the performance statistics for $OM_{2.5}$ and OM_{10} concentrations, turning an underprediction on both days into an overprediction on August 27 and a lower underprediction on August 28. The predicted mean $OM_{2.5}$ concentrations averaged over 8 PM sampling sites increased from 7.3 to 11.3 μg m^{-3} on August 27 and 6.8 to 9.0 μg m^{-3} on August 28. For comparison, the observed $OM_{2.5}$ concentrations were 9.4 and 11.4 μg m^{-3} on August 27 and 28, respectively. The predicted mean error and bias with MADRID 2 are 46% and 34% on August 27 and 53% and -7% on August 28 for $OM_{2.5}$. The higher SOA predictions by MADRID 2 can be attributed to several factors: (1) more condensable organic products are treated in MADRID 2; (2) hydrophilic compounds, in addition to hydrophobic compounds, are treated in MADRID 2 but not in MADRID 1. Those hydrophilic condensable compounds formed primarily at night due to high RHs, they contributed about 5-15% of SOA formation on daily average; (3) larger (by roughly a factor of 2) partition coefficients employed in MADRID 2 than those in MADRID 1.

4.5.3 Sensitivity to condensational growth algorithms

A sensitivity simulation was conducted with 8 size sections and a simple finite-difference approach (i.e., a semi-Lagrangian technique) for particle growth and the results were compared to the base case results with the moving-center scheme to demonstrate the model

sensitivity to different particle growth schemes. In both simulations, the CMU hybrid approach was used to simulate gas/particle mass transfer. The simple finite difference scheme used here is based on that in the 1998 version of CIT [*Meng et al.*, 1998], which was coupled with the CIT bulk equilibrium approach or the simple bulk equilibrium approach to approximate mass transfer in CIT. In this simple finite-difference approach, the particle mass concentration after condensation or volatilization is adjusted using a factor that is calculated based on an incremental particle diameter corresponding to the incremental change in the particle mass (or volume) concentration. A fundamental difference between the moving-center scheme and the finite-difference scheme is that the former predicts both PM mass and number concentrations, whereas the latter predicts only the PM mass concentrations and diagnoses the PM number concentrations from the predicted PM mass and the fixed PM mean diameters.

The particle size distribution predicted by the moving-center and the finite-difference schemes is shown at HAWT, LBCC, CELA and BURK on August 27 in Figure 10 and at CLAR and RIVR on August 28 in Figure 7 along with the observed average particle size distribution during the SCAQS summer sampling periods. The particle size distribution is obtained by summing those for all PM compositions (i.e., SO_4^{2-}, NO_3^-, NH_4^+, Na^+, Cl^-, EC, OM and OI) in Figure 10 and all but Na^+, Cl^- and OI in Figure 7. The finite-difference scheme tends to predict a diffusive type of distribution for $PM_{2.5}$, with high concentrations in size sections 1 and 2 (0.0215-0.0464 μm and 0.0464-0.1 μm, respectively) (i.e., upstream diffusion) at both sites. The moving-center scheme predicts either one or two modes, with a $PM_{2.5}$ concentration peak in size sections 3 or 4 (0.1-0.215 μm and 0.215-0.464 μm). The PM mass fractions in the first size section (0.0215-0.0464 μm) predicted by the finite-difference scheme account for 10 to 30% total $PM_{2.5}$ at the 8 PM sampling sites, which is significantly higher than those with the moving-center scheme (i.e., 0.02 to 0.2%). For comparison, the observed PM

mass concentrations below 0.05 μm during the 1987 SCAQS study were negligible [e.g., *Wall et al.*, 1988; *John et al.*, 1990; *Hering et al.*, 1997; *Meng et al.*, 1998; and *Kleeman and Cass*, 1998]. Accordingly, the finite-difference scheme severely underpredicts a PM mass concentration of accumulation mode particles. In contrast, the moving-center scheme predicts a size distribution that is closer to the observed one in terms of the magnitudes and general shape of size-resolved PM composition, although the peak PM mass is somewhat underpredicted and is off the observed size for peak PM mass. The finite-difference scheme moves mass from section to section during each timestep, causing significant numerical diffusion. Whereas, the moving-center scheme only moves mass from section to section when the section center grows out of the section, therefore minimizing the numerical diffusion.

The numerical diffusion of the finite-difference scheme artificially increases the 24-hr average $PM_{2.5}$ and PM_{10} mass at many sites on both days. Compared to the base results, the 24-hr average mass concentrations of $PM_{2.5}$ predicted by the finite-difference scheme increase significantly (by 8-30%) at all sites except the two downwind sites (CLAR and RIVR) on August 27. The mass concentrations of PM_{10} also increase accordingly (by 8-27%) at ANAH, AZUS, BURK, HAWT and LBCC on both days and CELA on August 27. The increase in mass concentrations in the first two sections significantly increases the concentrations of particle number and the surface area available for heterogeneous reactions, which in turn led to a significant increase in the heterogeneous reaction rates of HO_2, NO_2, NO_3, and N_2O_5 and the mixing ratios of relevant gas-phase species including H_2O_2, NO_2, O_3, NO, HNO_3, OH and HO_2 at these locations. For example, at LBCC, the particle number concentrations and H_2O_2 mixing ratios increased by 46-80% and 11-65%, respectively. The HNO_3 mixing ratios decreased by up to a factor of 3.9 at night, then increased by up to 16% between sunrise and noon. The O_3

mixing ratios increased by up to 10% (13.1 ppb) in the morning but decreased in the afternoon by up to 10% (11.4 ppb).

4.5.4 Sensitivity to gas-to-particle mass transfer approaches

Figure 11 compares the total particle mass size distribution predicted with the CMU hybrid, the CIT bulk and a simple bulk equilibrium approaches at HAWT and CELA on both days. A similar comparison is shown in Figure 7 at CLAR and RIVR on August 28 along with the observed average particle size distribution during the summer sampling periods. Although the simple bulk equilibrium approach gave mass concentrations for PM_{10} and its components similar to those of the CIT bulk equilibrium approach, it predicted a diffusive type of distribution, with lower mass concentrations in sections 2-5 between 0.1 –1.0 μm, but much higher concentrations in larger sections, particularly in sections 6 and 8 (i.e., downstream diffusion). The total mass size distributions predicted by the CIT bulk equilibrium and the CMU hybrid approaches are quite similar (i.e., with similar amount of mass in each section and the peak occurring in the same section) at CLAR and ANAH (not shown) on August 27 and AZUS (not shown), BURK (not shown), CELA, CLAR (see Figure 7) and HAWT on August 28. They both predicted a two-mode distribution at BURK (see Figure 10 (d)) and HAWT on August 27 and a one-mode distribution at RIVR on August 27-28 (e.g., see Figure 7) and ANAH (not shown) and LBCC (not shown) on August 28, although the mass concentrations in each section were somewhat different and the peak concentrations occurred in different sections. The CMU hybrid approach predicted a two-mode distribution at CELA and LBCC (not shown) with peaks in sections 3 and 6 (0.1-0.215 μm and 1.0-2.15 μm, respectively) on August 27, whereas the CIT bulk equilibrium approach predicted a one-mode distribution at these locations with the peak in sections 4 and 3 at the two locations, respectively. Compared

to the CIT bulk equilibrium approach, the CMU hybrid approach treats the gas/particle mass transfer explicitly for coarse particles, predicting higher mass concentrations in coarse sections, which in turn affects the mixing ratios of gas-phase species that are in equilibrium with the fine size sections. Although both approaches distribute the particle mass changes into fine size sections based on particle surface area weighting, the equations for the calculation of the weighting factors are somewhat different; in particular, the mass accommodation coefficient used in the CMU hybrid approach is 0.1, which is a factor of 10 higher than that used in the CIT bulk equilibrium approach. Therefore, the CMU hybrid approach tends to give more weight to smaller size sections, with a peak concentration occurring most likely in smaller sections than the CIT bulk equilibrium approach at many sites such as BURK, CELA, HAWT, AZUS, CLAR and LBCC.

The CMU hybrid approach and the CIT bulk equilibrium approach predicted quite different mass size distributions of individual components, as shown in Figure 12. Both approaches predict a two-mode distribution for SO_4^{2-} with similar total mass and the same peak sections (i.e., between 0.1-0.215 μm and 0.464-1.0 μm), but the highest sulfate mass concentration occurred between 0.1-0.215 μm for the CMU hybrid approach and between 0.464-1.0 μm for the CIT bulk equilibrium approach. Both approaches predict similar total mass of NH_4^+ but with a more spread-out distribution over size sections in the CIT bulk equilibrium approach. Both approaches predict similar mass of Na^+ in section 8 (4.64 – 10 μm), but the CMU hybrid approach predict higher mass concentrations of Cl^- than those of the CIT bulk equilibrium approach (0.19 vs. 0.01 μg m^{-3} at HAWT and 0.6 vs. 0.13 μg m^{-3} at CELA), which are in better agreement with the observed values of 1.0 and 0.7 μg m^{-3} at HAWT and CELA, respectively.

The most significant differences between the two approaches lie in the total mass and size distribution of NO_3^-. The CMU hybrid approach predicts a much higher total NO_3^- mass than the CIT bulk equilibrium approach (6.8 vs. 1.9 μg m^{-3} at HAWT and 13.9 vs. 9.9 μg m^{-3} at CELA, respectively). As a result of a larger total mass with a faster growth rate in fine sections and an explicit mass transfer in coarse sections, the CMU hybrid approach predicts higher mass concentrations for both fine and coarse NO_3^- than the CIT bulk equilibrium approach. For example, the mass concentrations of coarse NO_3^- predicted by the CMU hybrid and CIT bulk equilibrium approaches are 1.5 and 0.19 μg m^{-3} at HAWT and 1.93 and 0.77 μg m^{-3} at CELA, respectively, on August 27. For comparison, the observed mass concentrations of coarse NO_3^- ($nitrate_{10-2.5}$) are 0.73 and 1.0 μg m^{-3} at HAWT and CELA, respectively. Note that the observed $nitrate_{10-2.5}$ mass concentrations are obtained by subtracting the observed $nitrate_{2.5}$ mass from the observed $nitrate_{10}$ mass and they may be underestimated, due to mass losses occurring during $nitrate_{10}$ sampling with the Teflon filter method. Therefore, the accuracy in $nitrate_{10}$ predicted by the CMU hybrid and CIT bulk equilibrium approaches can not be determined because of the uncertainties in the nitrate measurements. It is clear that the CIT bulk equilibrium approach tends to underpredict the mass concentrations of coarse nitrate and chloride at or near coastal sites; it is however applicable for ambient conditions with low concentrations of coarse sea salt and alkaline dust particles.

Despite the above differences, both the CMU hybrid and the CIT bulk equilibrium approaches can predict particle size distribution for $PM_{2.5}$ that is reasonably close to the observed size distribution as shown in Figure 7, considering the large uncertainties in meteorology and emissions inventories used, a relatively coarse size resolution of 8 size sections used and difficulties in accurately simulating particle size distribution due to many complex microphysical processes that govern PM chemical composition and size distribution.

One limitation is that both the CIT bulk equilibrium and the CMU hybrid approaches employ equilibrium assumptions on gas/particle mass transfer (except for coarse particles in the CMU hybrid approach). The dynamic approach that explicitly treats mass transfer [e.g., *Meng et al.*, 1996, 1998; *Jacobson*, 1997a, 1997b; *Sun and Wexler*, 1998a, 1998b] should give more accurate results in theory than both simplified approaches but will require higher computational costs. Such an explicit mass transfer approach should be used when computational resources are available.

5. CONCLUSION

We have presented the development and initial application of a new 3-D air quality model for PM, CMAQ-MADRID. This model combines a state-of-the-science representation of the major processes that govern the chemical composition and size distribution of PM in the atmosphere with numerical robustness of the corresponding algorithms.

CMAQ-MADRID was applied to simulate an air pollution episode in the Los Angeles basin. Model performance for both O_3 and PM predictions was shown to be consistent with existing guidance. The model simulations reproduce the magnitude and the spatial and temporal variations of O_3 mixing ratios throughout the basin, but tend to overpredict daytime O_3 mixing ratios at a few sites in the western basin on August 27 and underpredict the O_3 mixing ratios at inland sites downwind on August 28. The overpredictions or underpredictions are due, at least in part, to mispredictions in the meteorological inputs such as wind speeds and vertical mixing. The evolution of the chemical composition of PM from the coastal areas to the inland areas was well reproduced except that EC and OM were underpredicted and particulate nitrate formation was sometimes underpredicted. The underprediction in EC may be due to uncertainties in meteorological inputs, EC emissions and the size distribution of

emitted EC. The underpredictions in OM may be due to uncertainties in meteorological inputs, emissions of condensable VOC species and primary OC emissions, the partition coefficient used for condensable SOA precursors, as well as an incomplete inclusion of the condensable VOC species that contribute to SOA formation. The underpredictions in nitrate are due mainly to overpredictions in vertical mixing, underpredictions in RH and uncertainties in the emissions of primary pollutants such as VOC, NO_x and NH_3. These results indicate the importance of accurate meteorological inputs, emissions (both gases and primary PM species), characterization of emitted PM size distribution as well as model representation of various atmospheric processes for PM air quality simulations.

The sensitivity of model predictions was evaluated with respect to several major areas of uncertainties in PM modeling including the treatment of heterogeneous reactions, and different modules/algorithms for SOA formation, particle growth due to condensation (or shrinkage due to volatilization) and gas/particle mass transfer. The predicted gas-phase species mixing ratios and particulate-phase species concentrations are sensitive to heterogeneous reactions of HO_2, NO_2, NO_3 and N_2O_5 on particles and droplets. Heterogeneous reactions taking place at the surface of particles and droplets are shown to potentially affect hourly O_3 mixing ratios by up to 17% and hourly concentrations of $sulfate_{10}$, $ammonium_{10}$, and $nitrate_{10}$ by up to 21%, 25%, and a factor of 12, respectively. Such an effect may even cause changes in 24-hr average $PM_{2.5}$, PM_{10} and their compositions (e.g., up to 3%, 7% and 19% for 24-hr average $PM_{2.5,}$ $sulfate_{2.5}$ and $nitrate_{2.5}$ concentrations). Uncertainties are associated with the reaction probabilities of the simulated heterogeneous reactions and the particle and droplet surface areas used.

The treatment of SOA formation was investigated with a sensitivity simulation. A SOA module with a mechanistic representation (i.e., MADRID 2) provides OM concentrations

that are in better agreement with observations than a SOA module that is based on smog chamber data (i.e., MADRID 1). The treatment of SOA formation is still an area of ongoing research and large uncertainties currently exist for this PM component in all existing air quality models. The yields of condensable organic compounds and the temperature-dependent gas/particle partition coefficients of those compounds are still major sources of uncertainties that will require additional fundamental studies to improve our ability to predict SOA concentrations.

The predicted fine and total particle mass and their size distributions are sensitive to the numerical algorithms for simulation of particle growth and gas/particle mass transfer. The moving-center scheme for particle growth is shown to predict more accurate particle size distributions than other semi-Lagrangian and Lagrangian schemes such as the finite-difference scheme, which typically cause an upstream numerical diffusion. For gas/particle mass transfer, a realistic particle size distribution can be predicted with the CMU hybrid approach under most ambient conditions and with the CIT bulk equilibrium approach under conditions with negligible reactive coarse particles (e.g., sea salt and dust). In contrast, the simple bulk equilibrium approach tends to cause a downstream numerical diffusion in the predicted particle size distribution. These sensitivity simulations demonstrate a need for careful selection of numerical algorithms for simulating PM thermodynamics and dynamics for 3-D air quality models that are based on a sectional representation of the particle size distribution.

Accurate model inputs (e.g., emissions and meteorology), realistic representations of various atmospheric processes (e.g., SOA formation), appropriate numerical algorithms for PM dynamics (e.g., condensational growth and gas/particle mass transfer) and fine particle size resolution (e.g., > 8 size sections) will greatly reduce the major model uncertainties and thus improve the accuracy for 3-D PM modeling.

ACKNOWLEDGEMENTS

This work was conducted under funding from EPRI under Contract EP-P2542/C1151. We thank the EPRI Project Managers, Dr. Naresh Kumar and Dr. Alan Hansen, for their continuous support.

6. REFERENCES

Allen, P.D., and K.K. Wagner, *1987 SCAQS Emission Inventory, magnetic tape numbers ARA806 and ARA807*; Technical Support Division, California Air Resources Board: Sacramento, CA, 1992.

Ansari A., and S. N. Pandis, An analysis of four models predicting the partitioning of semivolatile inorganic aerosol components, *Aerosol Sci. Tech., 31*, 129-153, 1999.

Bilde, M., and S.N. Pandis, Evaporation rates and vapor pressures of individual aerosol species formed in the atmospheric oxidation of α- and β-Pinene, *Environ. Sci. Technol., 35*, 3344-3349, 2001.

Binkowski, F.S., and U. Shankar, The regional particulate matter model. 1: Model description and preliminary results, *J. Geophys. Res., 100*, 26191-26209, 1995.

Binkowski, F.S., Aerosols in Models-3 CMAQ, Chapter 10, in *Science Algorithms of the EPA Models-3 Community Multiscale Air Quality [CMAQ] Modeling System*, D.W. Byun and J.S. Ching, eds., EPA/600/R-99/030, Office of Research and Development, U.S. Environmental Protection Agency, Washington, D.C.,1999.

Bott, A., A positive definite advection scheme obtained by nonlinear renormalization of the advective fluxes, *Mon. Wea. Rev., 117*, 1006-1015, 1989.

Bowman, F.M., C. Pilinis, and J.H. Seinfeld, Ozone and aerosol productivity of reactive organics, *Atmos. Environ., 29*, 579-589, 1995.

Byun, D.W., and J.K.S. Ching, *Science Algorithms of the EPA Models-3 Community Multiscale Air Quality [CMAQ] Modeling System*, EPA/600/R-99/030, Office of Research and Development, U.S. Environmental Protection Agency, Washington, D.C.,1999.

Capaldo, K.P., C. Pilinis, and S.N. Pandis, A computationally efficient hybrid approach for dynamic gas/aerosol transfer in air quality models, *Atmos. Environ.*, *34*, 3617-3627, 2000.

Carter, W.P.L., *Documentation of the SAPRC-99 chemical mechanism for VOC reactivity assessment*, Final report to California Air Resources Board, Contract 92-329 and Contract 95-308, 2000.

Cass, G.R., and S. Gharib, Ammonia emissions in the South Coast Air Basin, 1982, Open File Rep. 84-2, Environ. Qual. Lab., Calif. Inst. of Technol., Pasadena, Calif., 1984.

Cheung, J. L., Y. Q. Li, J. Boniface, Q. Shi, and P. Davidovits, Heterogeneous interactions of NO_2 with aqueous surfaces, *J. Phys. Chem.*, *104*, 2655-2662, 2000.

Chock, D.P., and S.L. Winkler, A trajectory-grid approach for solving the condensation and evaporation equations of aerosols, *Atmos. Environ.*, *34*, 2957-2973, 2000.

Clegg, S.L., P. Brimblecombe, and A.S. Wexler, A thermodynamic model of the system H^+ -NH_4^+ -Na^+ -SO_4^{2-} -NO_3^- -Cl^- -H_2O at 298.15 K, *J. Phys. Chem.*, 102, 2155-2171, 1998a.

Clegg, S.L., P. Brimblecombe, and A.S. Wexler, A thermodynamic model of the system H^+ -NH_4^+ -Na^+ -SO_4^{2-} -NO_3^- -Cl^- -H_2O at tropospheric temperatures, *J. Phys. Chem.*, *102*, 2137-2154, 1998b.

Dassios, K.G., and S.N. Pandis, The mass accommodation coefficient of ammonium nitrate aerosol, *Atmos. Environ.*, *33*, 2999-3003, 1999.

Eldering, A., and G.R. Cass, Source-oriented model for air pollutant effects on visibility, *J. Geophys. Res., 101*, 19,343-19,369, 1996.

Fahey, K.M., and S.N. Pandis, Optimizing model performance: Variable size resolution in cloud chemistry modeling, *Atmos. Environ., 35*, 4471-4478, 2001.

Fitzgerald, J.W., W.A. Hoppel, and F. Gelbard, A one-dimensional sectional model to simulate multicomponent aerosol dynamics in the marine boundary layer. 1. Modal description, *J. Geophys. Res., 103*, 16085-16102, 1998.

Fraser, M.P., D. Grosjean, E. Grosjean, R.A. Rasmussen, and G.R. Cass, Air quality model evaluation data for organics. !. Bulk chemical composition and gas/particle distribution factors, *Environ. Sci. Technol., 30*, 1731-1743, 1996.

Gery, M.W., G.Z. Whitten, J.P. Killus, and M.C. Dodge, A photochemical kinetics mechanism for urban and regional scale computer modeling, *J. Geophys. Res., 94*, 12,925-12,956, 1989.

Gillani, N.V., S.E. Schwartz, W.R. Leaitch, J.W. Strapp, and G.A. Isaac, Field observations in continental stratiform clouds: Partitioning of cloud particles between droplets and unactivated interstitial aerosols, *J. Geophys. Res., 100*, 18,687-18,706, 1995.

Gipson G.L., and J.O. Young, Gas-Phase Chemistry, Chapter 8, in *Science Algorithms of the EPA Models-3 Community Multiscale Air Quality [CMAQ] Modeling System,* D.W. Byun and J.S. Ching, eds., EPA/600/R-99/030, Office of Research and Development, U.S. Environmental Protection Agency, Washington, D.C.,1999.

Griffin, R.J., D.R. Cocker III, R.C. Flagan, and J.H. Seinfeld, Organic aerosol formation from the oxidation of biogenic hydrocarbons, *J. Geophys. Res., 104*, 3555-3567, 1999.

Griffin, R.J., D. Dabdub, M.J. Kleeman, M.P. Fraser, G.R. Cass, and J.H. Seinfeld, Secondary organic aerosol: III. Urban/regional scale model of size- and composition-resolved aerosols, *J. Geophys. Res.*, *107*[D17], ??, doi:10.1029/2001JD000544, 2002.

Harley, R., A.G. Russell, G.J. McRae, G.R. Cass, and J.H. Seinfeld, Photochemical modeling of the Southern California Air Quality Study, *Environ. Sci. Technol., 27*, 378-388, 1993.

Harley, R., R.F. Sawyer, and J.B. Milford, Updated photochemical modeling for California South Coast Air Basin: Comparison of chemical mechanisms and motor vehicle emission inventories, *Environ. Sci. Technol., 31*, 2829-2839, 1997.

Hegarty, J., M. Leidner, and M. Iacono, Modeling air pollution in the Los Angeles Basin using the MM5-SAQM modeling system. Part I: meteorological simulations. In *Proceedings of the 10th Joint Conference on the Applications of Air Pollution Meteorology with the A&WMA*; Phoenix, AZ, January 11-16, 1998.

Harrington, D. Y., and S. M. Kreidenweis, Simulation of Sulfate Aerosol Dynamics. I. Model Description. *Atmos. Environ.*, *32*, 1691-1700, 1998.

Hering, S. A. Eldering, and J.H. Seinfeld, Bimodal character of accumulation mode aerosol mass distributions in southern California, *Atmos. Environ.*, 31, 1-11, 1997.

Hudischewskyj, A. B. and C. Seigneur, Mathematical Modeling of the Chemistry and Physics of Aerosols in Plumes. *Environ. Sci. Technol. 23*, 413-421, 1989.

Jacob, D., Heterogeneous chemistry and tropospheric ozone, *Atmos. Environ., 34*, 2132-2159, 2000.

Jacobson, M.Z., R. Lu, P.R. Turco, and O.B. Toon, Development and application of a new air pollution modeling system – I. Gas-phase simulations, *Atmos. Environ., 30B*, 1939-1963, 1996.

Jacobson, M.Z., Development and application of a new air pollution modeling system – II. Aerosol module structure and design, *Atmos. Environ.*, *31*, 131-144, 1997a.

Jacobson, M.Z., Development and application of a new air pollution modeling system – part III. Aerosol-phase simulations, *Atmos. Environ.*, *31*, 587-608, 1997b.

Jacobson, M.Z., Studying the effects of calcium and magnesium on size-distributed nitrate and ammonium with EQUISOLV II, *Atmos. Environ.*, *33*, 3635-3649, 1999.

Jacobson, M. Z., Analysis of aerosol interactions with numerical techniques for solving coagulation, nucleation, condensation, dissolution, and reversible chemistry among multiple size distributions, *J. Geophys. Res*., *107* [D19], 4366, doi:10.1029/ 2001JD002044, 2002.

John, W., S.M. Wall, J.L. Ondo, and W. Winklmayr, Modes in the size distributions of atmospheric inorganic aerosol, *Atmos. Environ.*, *24A*, 2349-2359, 1990.

Kleeman, M.J., G.R. Cass, and A. Eldering, Modeling the airborne particle complex as a source-oriented external mixture, , *J. Geophys. Res*., *102* 21,355-21,372, 1997.

Kleeman, M.J., and G.R. Cass, Source contributions to the size and composition distribution of urban particulate air pollution, *Atmos. Environ.*, *32*, 2803-2816, 1998.

Kim, Y.P., and J.H. Seinfeld, Atmospheric gas-aerosol equilibrium III: thermo-dynamics of crustal elements Ca^{2+}, K^{+}, and Mg^{2+}, *Aerosol Sci. Technol.*, *22*, 93-110, 1995.

Koo, B., T.M. Gaydos, and S.N. Pandis, Evaluation of the equilibrium, dynamic, and hybrid aerosol modeling approaches, *Aerosol Sci. Technol.*, *37*, 53-64, 2003.

Lamb, B., D. Grosjean, B. Pun, and C. Seigneur, *Review of the emissions, atmospheric chemistry, and gas/particle partition of biogenic volatile organic compounds and reaction products*, Final Report, Coordinating Research Council, Alpharetta, GA, NTIS PB2000-192875, 1999.

Leaitch, W.R., Observations pertaining to the effect of chemical transformation in cloud on the anthropogenic aerosol size distribution, *Aerosol Sci. Technol.*, *25*, 157-173, 1996.

Liu, P.S.K., W.R. Leaitch, C.M. Banic, S.M. Li, D. Ngo, and W.J. Megaw, Aerosol observations at Chebogue Point during the 1993 North Atlantic Regional Experiment: Relations among cloud condensation nuclei, size distribution, and chemistry, *J. Geophys. Res.*, *101*, 28971-28990, 1996.

Lu, R., R.P. Turco, and M.Z. Jacobson, An integrated air pollution modeling system for urban and regional scales: 2. Simulations for SCAQS 1987, *J. Geophys. Res.*, *102*, 6081-6098, 1997.

Lurmann, F.W., A.S. Wexler, S.N. Pandis, S. Musarra, N. Kumar, and J.H. Seinfeld, Modeling urban and regional aerosols - II. Application to California's south coast air basin, *Atmos. Environ.*, *31*, 2695-2715, 1997.

McMurry, P.H., and S.K. Friedlander, New particle formation in the presence of an aerosol, *Atmos. Environ.*, *13*, 1635-1651, 1979.

Meng, Z., J.H. Seinfeld, P. Saxena, and Y.P. Kim, Atmospheric gas-aerosol equilibrium, IV: thermodynamics of carbonates, *Aerosol Sci. Technol.*, *23*, 131-154, 1995.

Meng, Z., and J.H. Seinfeld, Time scales to achieve atmospheric gas-aerosol equilibrium for volatile species, *Atmos. Environ.*, *30*, 2889-2900, 1996.

Meng, Z., D. Dabdub, and J.H. Seinfeld, Size-resolved and chemically resolved model of atmospheric aerosol dynamics, *J. Geophys. Res.*, *103*, 3419-3435, 1998.

Moya, M., S.N. Pandis, and M.Z. Jacobson, Is the size distribution of urban aerosols determined by thermodynamic equilibrium? An application to Southern California, *Atmos. Environ.*, *36*, 2349-2365, 2002.

Middleton, P., DAQM-simulated spatial and temporal differences among visibility, PM, and other air quality concerns under realistic emission change scenarios, *J. Air Waste Manage. Assoc.*, *47*, 302-316, 1997.

Nenes, A., S.N. Pandis, and C. Pilinis, ISORROPIA: A new thermodynamic equilibrium model for multiphase multicomponent inorganic aerosols, *Aquatic Geochemistry*, *4*, 123-152, 1998.

Nenes, A., C. Pilinis, and S.N. Pandis, Continued development and testing of a new thermodynamic aerosol module for urban and regional air quality models, *Atmos. Environ.*, *33*, 1553-1560, 1999.

Nguyen, K., and D. Dabdub, Semi-Langrangian flux scheme for the solution of the aerosol condensation/evaporation equation, *Aerosol Sci. Technol.*, *36*, 407-418, 2002.

Odum, J.R., T.P.W. Jungkamp, R.J. Griffin, H.J.L. Forstner, R.C. Flagan, and J.H. Seinfeld, Aromatics, reformulated gasoline, and atmospheric organic aerosol formation, *Environ. Sci. Technol.*, *31*, 1890-1897, 1997.

Pai, P., K. Vijayaraghavan, and C. Seigneur, Particulate matter modeling in the Los Angeles Basin using SAQM-AERO, *J. Air Waste Manage. Assoc.*, *50*, 32-42, 2000.

Pandis, S.N., and J.H. Seinfeld, Sensitivity analysis of a chemical mechanism for aqueous-phase atmospheric chemistry, *J. Geophys. Res.*, *94*, 1105-1126, 1989.

Pandis, S.N., R.A. Harley, G.R. Cass, and J.H. Seinfeld, Secondary organic aerosol formation and transport, *Atmos. Environ.*, *26A*, 2269-2282, 1992.

Pandis, S.N., A.S. Wexler, and J.H. Seinfeld, Secondary organic aerosol formation and transport-II. Predicting the ambient secondary organic aerosol size distribution, *Atmos. Environ.*, *27A*, 2403-2416, 1993.

Pandis, S.N., L.M. Russell, and J.H. Seinfeld, The relationship between DMS flux and CCN concentration in remote marine regions, *J. Geophys. Res.*, 99, 16945-16957, 1994.

Pankow, J.F., An absorption model of the gas/aerosol partition involved in the formation of secondary organic aerosol, *Atmos. Environ., 28,* 189-193, 1994.

Pilinis, C., K.P. Capaldo, A. Nenes, and S.N. Pandis, MADM-A new multicomponent atmospheric aerosols, *Aerosol Sci. and Tech., 32*, 482-502, 2000.

Pilinis, C., and J.H. Seinfeld, Continued development of a general equilibrium model for inorganic multicomponent atmospheric aerosols, *Atmos Environ., 32*, 2453-2466, 1987.

Pruppacher, H.R., and J.D. Klett, *Microphysics of Clouds and Precipitation*, 714 pp., D. Reidel, Norwell, Mass., 1980.

Pun, B.K., R.J. Griffin, C. Seigneur, and J.H. Seinfeld, Secondary organic aerosol: II. Thermodynamic model for gas/particle partitioning of molecular constituents, *J. Geophys. Res., 107*[D17], 4333, doi:10.1029/2001JD000542, 2002.

Pun, B., S.-W. Wu, C. Seigneur, J.H. Seinfeld, R.J. Griffin and S.N. Pandis, Uncertainties in modeling secondary organic aerosols: three-dimensional modeling studies in Nashville/Western Tennessee, *Environ. Sci. Technol.*, in press, 2003.

RAQC, Development of the Denver Air Quality Model - Version 2, Final Report by the RAQC to the State of Co. Office of Energy Conservation, 1999.

Roselle, S.J., and F.S. Binkowski, Cloud Dynamics and Chemistry, Chapter 11, in *Science Algorithms of the EPA Models-3 Community Multiscale Air Quality [CMAQ] Modeling System,* D.W. Byun and J.S. Ching, eds., EPA/600/R-99/030, U.S. Environmental Protection Agency, Washington, D.C., 1999.

Seigneur, C., A model of sulfate aerosol dynamics in atmospheric plumes, *Atmos. Environ., 16,* 2207-2228, 1982.

Seigneur, C., Current status of air quality modeling for particulate matter, *J. Air Waste Manage. Assoc.*, *51*, 1508-1521, 2001.

Seigneur, C., and M. Moran, Chemical transport models, Chapter 8 in *Particulate Matter Science for Policy Makers, A NARSTO PM Assessment, Electric Power Research Institute*, Palo Alto, California, 2003, 1007735.

Seigneur, C., P. Karamchandani, P. Pai, K. Vijayaraghavan, K. Lohman, and S.Y. Wu, Model comparisons and application of Models-3/CMAQ APT. paper presented at 1st Annual Models-3 Workshop, Arlington, Virginia, 2000a.

Seigneur, C., P. Pai, P. Hopke, and D. Grosjean, Modeling atmospheric particulate matter, *Environ. Sci. Technol.*, *33*, 80A-84A, 1999.

Seigneur, C., B. Pun, P. Pai, J.F. Louis, P. Solomon, C. Emery, R. Morris, M. Zahniser, D. Worsnop, P. Koutrakis, W. White, and I. Tombach, Guidance for the performance evaluation of three-dimensional air quality modeling systems for particulate matter and visibility, *J. Waste Manage. Assoc.*, *50*, 588-599, 2000c.

Seigneur, C., C. Tonne, K. Vijayaraghavan, and P. Pai, Sensitivity of $PM_{2.5}$ source-receptor relationships to atmospheric chemistry and transport in a three-dimensional air quality model, *J. Air Waste Manage. Assoc.*, *50*, 428-435, 2000b.

Seigneur, C., X. A. Wu, E. Constantinou, P. Gillespie, R. W. Bergstrom, I. Sykes, A. Venkatram and P. Karamchandani, Formulation of a Second-Generation Reactive Plume and Visibility Model. *J. Air & Waste Manage. Assoc. 47*, 176-184, 1997.

Seinfeld, J.H., and S.N. Pandis, *Atmospheric Chemistry and Physics - From Air Pollution to Climate Change*, John Wiley & Sons, Inc., New York, NY, 1998.

Sheehan, P.E. and F.M. Bowman, The estimated effects of temperature on secondary organic aerosol concentrations, *Environ. Sci. Technol.*, *35*, 2129-2135, 2001.

Stockwell, W.R., P., Middleton, and J.S. Chang, The second generation regional acid deposition model chemical mechanism for regional air quality modeling, *J. Geophys. Res.*, *95*, 16,343-16,397, 1990.

Sun, Q., and A.S. Wexler, Modeling urban and regional aerosols-condensation and evaporation near acid neutrality, *Atmos. Environ.*, *32*, 3527-3531, 1998a.

Sun, Q., and A.S. Wexler, Modeling urban and regional aerosol near acid neutrality-application to the 24-25 June SCAQS episode, *Atmos. Environ.*, *32*, 3533-3545, 1998b.

Tao, Y., and P.H. McMurry, Vapor pressures and surface free energies of C14-C18 monocarboxylic acids and C5 and C6 dicarboxylic acids, *Environ. Sci. Technol.*, *23*, 1519-1523, 1989.

Venkatram, A., and J. Pleim, The electrical analogy does not apply to modeling dry deposition of particles, *Atmos. Environ.*, *33*, 3075-3076, 1999.

Walcek, C.J., and G.R. Taylor, A theoretical method for computing vertical distributions of acidity and sulfate production within cumulus clouds, *J. Atmos. Sci*., *43*, 339-355, 1986.

Wall, S.M., W. John, and J.L. Ondo, Measurement of Aerosol size distributions for nitrate and major ionic species, *Atmos. Environ.*, *22*, 1649-1656, 1988.

Wexler, A.S., and J.H. Seinfeld, The distribution of ammonium salts among a size and composition dispersed aerosol, *Atmos. Environ.*, *24A*, 1231-1246, 1990.

Wexler, A. S., F. W. Lurmann, and J. H. Seinfeld, Modeling Urban and Regional Aerosols. I. Model Development. *Atmos. Environ. 28*, 531-546, 1994.

White, W.H., and P.T. Roberts, On the nature and origins of visibility-reducing aerosols in the Los Angeles air basin, *Atmos. Environ.*, *11*, 803-812, 1977.

Zhang, Y., C. Seigneur, J.H. Seinfeld, M.Z. Jacobson, and F.S. Binkowski, Simulation of aerosol dynamics: A comparative review of algorithms used in air quality models, *Aerosol Sci. Technol.*, *31*, 487-514, 1999.

Zhang, Y., C. Seigneur, J.H. Seinfeld, M. Jacobson, S.L. Clegg, and F.S. Binkowski, A comparative review of inorganic aerosol thermodynamic equilibrium modules: similarities, differences, and their likely causes, *Atmos. Environ.*, *34*, 117-137, 2000.

Zhang, Y., Pun, B., K. Vijayaraghavan, S.-Y. Wu, and C. Seigneur, Community Multiscale Air Quality – Models of Aerosol Dynamics, Reaction, Ionization, and Dissolution (CMAQ-MADRID): Technical Documentation, *Electric Power Research Institute*, Palo Alto, California, 2002a, 1005239.

Zhang, Y., R.C. Easter, S.J. Ghan, and H. Abdul-Razzak, 2002b, Impact of Aerosol Size Representations on Modeling Aerosol-Cloud Interactions, *J. Geophys. Res.*, Vol. 107, 4558, doi:1029/2001JD001549.

List of Figures

Figure 7. Observed average particle size distribution during 1987 SCAQS summer sampling periods (taken from Hering et al. (1997)) and predicted size distribution of 24-hr average $PM_{2.5}$ concentrations on August 28, 1987 at (a) Claremont (CLAR) and (b) Riverside (RIVR) with various combinations of condensational growth algorithm and gas/particle mass transfer approach.

Figure 8. Predicted gas-phase mixing ratios of (a) HO_2, (b) H_2O_2, (c) HNO_3 and (d) O_3 at Hawthorne (HAWT) on August 27-28, 1987 with and without heterogeneous reactions.

Figure 9. Observed and predicted (with and without heterogeneous reactions) 24-hr average mass concentrations of $PM_{2.5}$ and its chemical compositions at Hawthorne (HAWT) on August 27, 1987.

Figure 10. The particle size distribution predicted by the moving-center and the finite-difference schemes at (a) Hawthorne (HAWT), (b) Long Beach (LBCC), (c) Central Los Angeles (CELA) and (d) Burbank (BURK) on August 27, 1987.

Figure 11. The total particle mass size distribution predicted with the CMU hybrid, the CIT bulk equilibrium and the simple bulk equilibrium approaches at Hawthorne (HAWT) ((a) and (b)) and Central Los Angeles (CELA) ((c) and (d)) on August 27-28, 1987.

Figure 12. The mass size distributions of Na^+, NH_4^+, $SO_4^=$, NO_3^- and Cl^- predicted by the CMU hybrid and the CIT bulk equilibrium approaches at HAWT ((a) and (b)) and CELA ((c) and (d)) on August 27, 1987.

Table 1. The parameterization of aerosol activation used in CMAQ-MADRID.

Particle Size Range, μm	**Fraction of Activation, F_{mass}**
For 6 or more sections between 0.02 and 10 μm:	
d_p[a] > 0.35	1.0
0.1 < d_p ≤ 0.35	0.5[b]
d_p ≤ 0.1	0.0
For 2-5 sections between 0.02 and 10 μm:	
d_p > 2.5	1.0
d_p ≤ 2.5	0.8[c]

(a) d_p denotes the low-bound aerodynamic diameter of each size section.

(b) The remaining 50% particle mass are activated according to $exp(-\beta \tau)$, where β is the mass scavenging coefficient for particles with 0.1 < d_p ≤ 0.35 μm, τ is the cloud lifetime.

(c) The remaining 20% particle mass are activated according to $exp(-\beta \tau)$, where β is the mass scavenging coefficient for particles with d_p ≤ 2.5 μm, τ is the cloud lifetime.

Table 2. Mean normalized gross errors (MNGE) and mean normalized biases (MNB) for 1-hr average O_3 and 24-hr average PM predictions averaged at all measurement sites on August 27 and 28, 1987[a].

	August 27		August 28		Other SCAQS Simulations	
Species	MNGE %	MNB %	MNGE %	MNB %	MNGE %	MNB %
O_3 [b]	36.2	20.3	31.0	-3.3	27.8 to 50[c, d, e]	-23 to 34[c, d, e]
$PM_{2.5}$ mass	41.5	30.1	46.9	-1.8	32 to 46[c, f, g]	-8 to 46[c, f, g]
PM_{10} mass	53.2	32.8	55.9	8.2	50.1 to 72 [c, f]	-9.3 to 72 [c, f]
$sulfate_{2.5}$	48.7	48.7	27.0	-27.0	28.4 to 48[c, f, g]	-30 to 3.7[c, f, g]
$sulfate_{10}$	35	31.6	35.4	-35.4	26.3 to 40[c, f]	2 to -8.3[c, f]
$ammonium_{2.5}$	61.3	61.3	43.6	-10.7	29 to 57[c, f, g]	-52.3 to 56[c, f, g]
$ammonium_{10}$	49.8	47.1	43.6	-19.2	23 to 45.7[c, f]	-0.2 to 12[c, f]
$nitrate_{2.5}$	28.9	-24.8	59.5	-50.7	18 to 67.8[c, f, g]	-20.7 to 47[c, f, g]
$nitrate_{10}$	24.9	-0.7	58.9	-26.6	15 to 69.8[c, f]	6 to 18.4[c, f]
$EC_{2.5}$	38.5	-17.2	69.7	-23.0	15 to 57.5[c, f, g]	-10 to 35 [c, f, g]
EC_{10}	37.0	-17.9	60.3	-34.1	34 to 50.6[c, f]	-15 to 16.2[c, f]
$OM_{2.5}$	38.4	-14.4	60.8	-28.2	38 to 49[c, f, g]	-44.1 to 14[c, f, g]
OM_{10}	53.6	16.9	64.6	-7.2	32 to 45.4[c, f]	0.3 to 5.8[c, f]
$sodium_{10}$	39.1	-35.2	36.9	-33.7	36 to 47[c, f]	-30.2 to 38[c, f]
$chloride_{10}$	49.2	-34.4	79.8	2.7	24 to 46.8[c, f]	16 to 24[c, f]

a. The MNGE and MNB are defined, respectively, as:

$$\frac{1}{N}\sum_{i=1}^{N}\frac{|P_i - O_i|}{O_i} \qquad \textit{and} \qquad \frac{1}{N}\sum_{i=1}^{N}\frac{(P_i - O_i)}{O_i}$$

where P_i and O_i are the predicted and observed 1-hr O_3 mixing ratios or 24-hr average particulate concentrations at location i for a specific date, and N is the total number of predicted and observed concentration pairs drawn from all sampling sites for the day [N=38 for O_3 and N=8 for $PM_{2.5}$, PM_{10} and their compositions].

b. A cut off mixing ratio of 40 ppb was used in the calculation of O_3 statistics in this work.

c. *Jacobson* [1997b], statistics are for average values over 38 O_3 sampling sites and 8 PM sampling sites for August 27-28, 1987. A cut off mixing ratio of 50 ppb was used in the calculation of O_3 statistics.

d. *Harley et al.* [1993], statistics are for average values over 37 O_3 sampling sites for August 28, 1987. A cut off mixing ratio of 60 ppb was used in the calculation of O_3 statistics.

e. *Harley et al.* [1997], statistics are for average values over 34 O_3 sampling sites for August 28, 1987. A cut off mixing ratio of 60 ppb was used in the calculation of O_3 statistics.

f. *Lurmann et al*. [1997], statistics are for 24-hr average values over 8 PM sampling sites for June 25, 1987.

g. *Meng et al.* [1998], statistics are for 24-hr average values over 8 PM sampling sites for August 28, 1987.

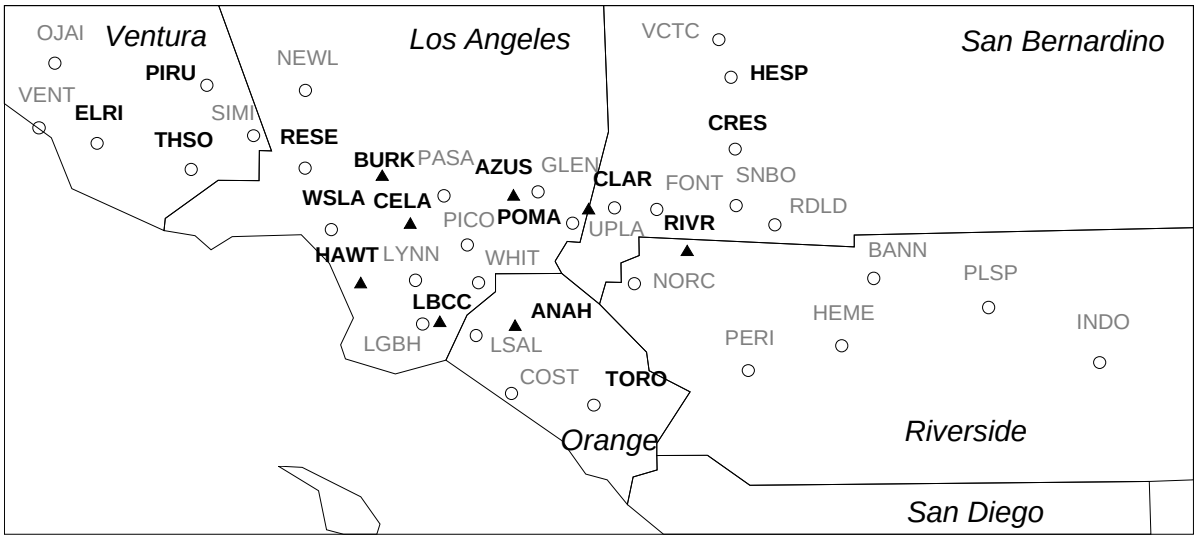

Figure 1. CMAQ-MADRID modeling domain and the locations of 38 O_3 measurement sites ("○") and 8 PM sampling sites ("▲") within the domain during SCAQS, 1987. The sites in bold are selected for a detailed analysis in this work.

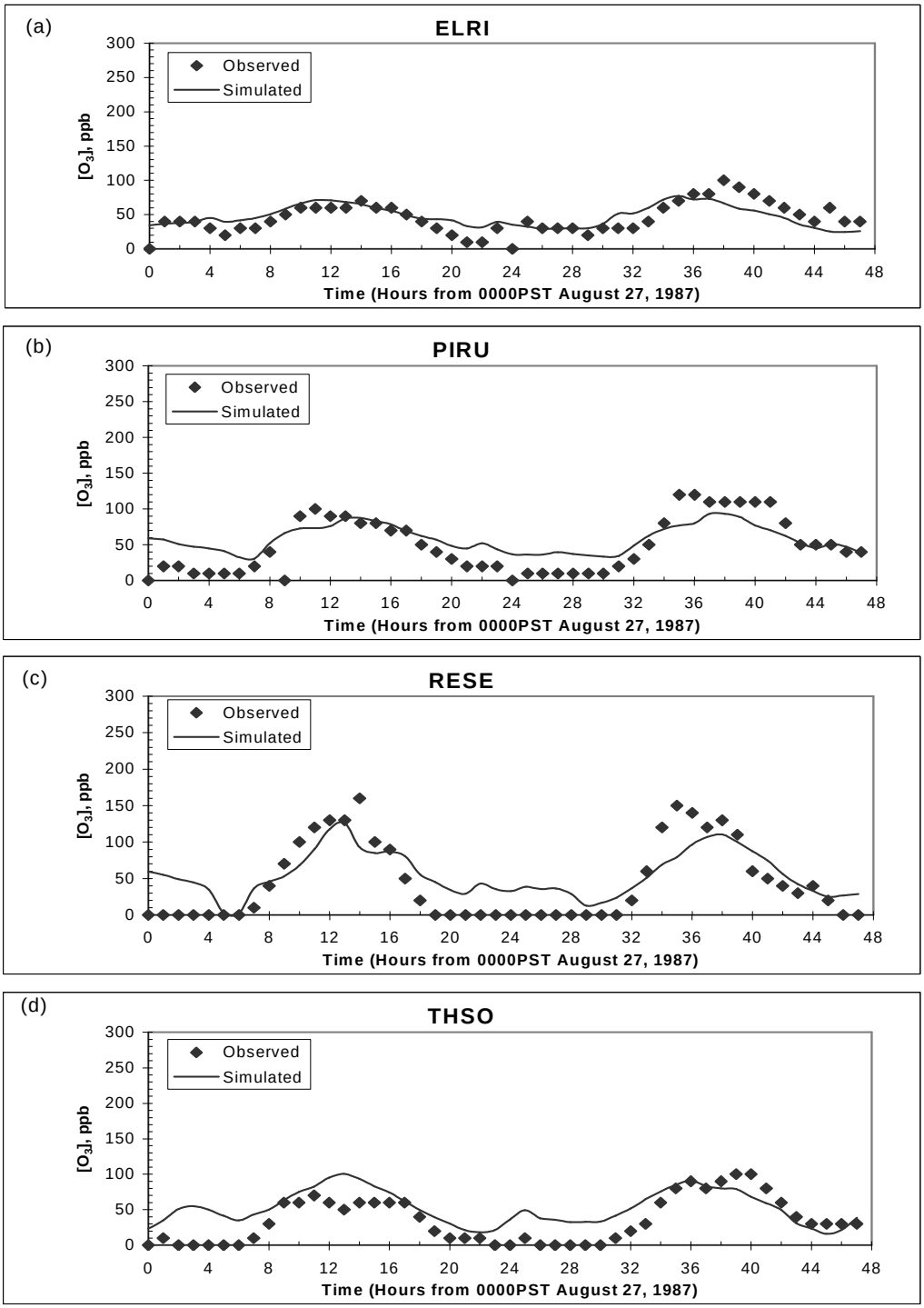

Figure 2. 2-day time series of observed and predicted O_3 mixing ratios at 12 monitoring sites selected to represent various parts of the basin. (a) El Rio (ELRI); (b) Piru (PIRU); (c) Reseda (RESE); (d) Thousand Oaks (THSO); (e) Central Los Angeles (CELA); (f) west Los Angeles (WSLA); (g) Pomona (POMA); (h) Riverside (RIVR); (I) Crestline (CRES); (j) Hesperia (HESP); (k) Long Beach (LBCC); (l) El Toro (TORO).

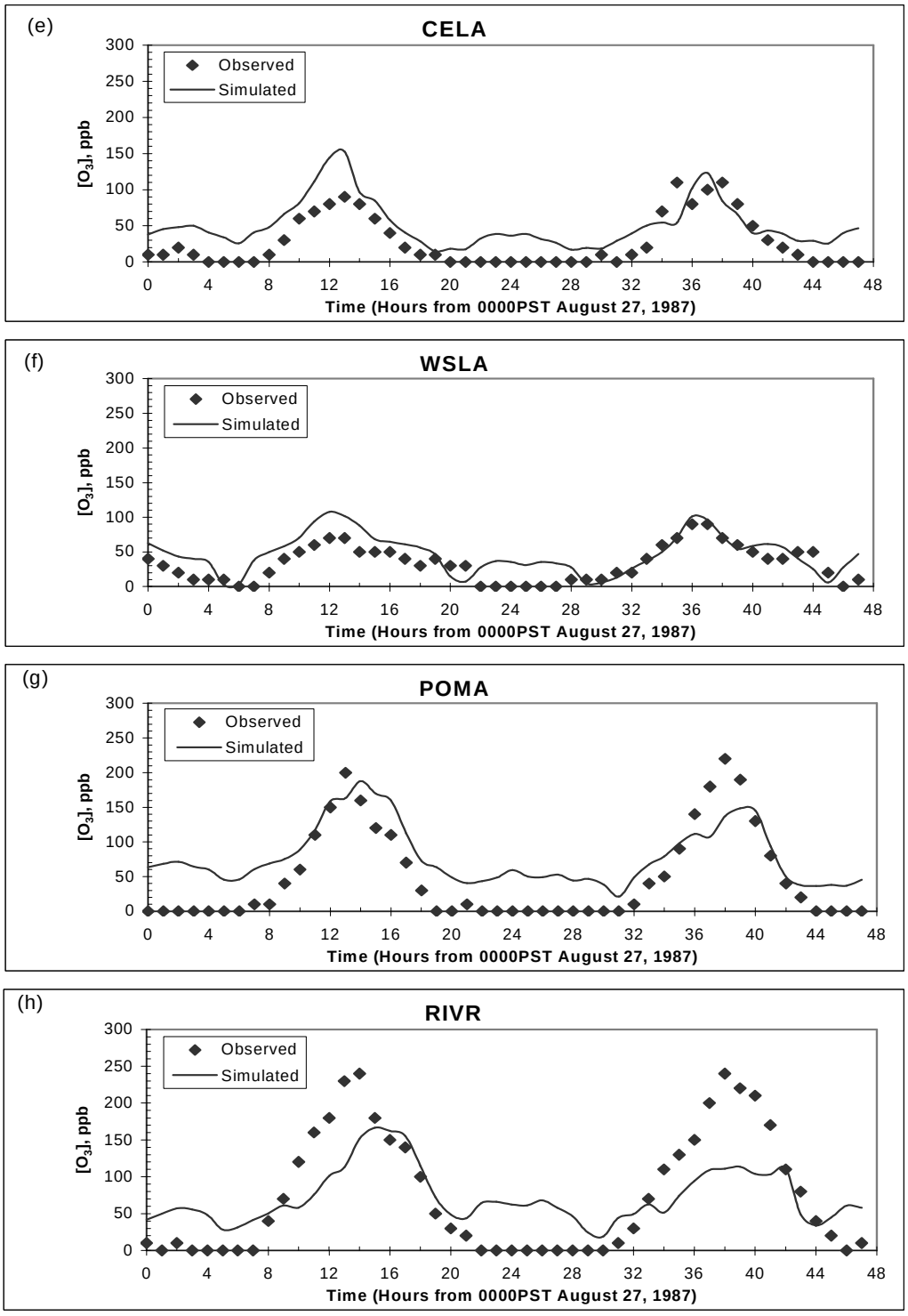

Figure 2 [con't]

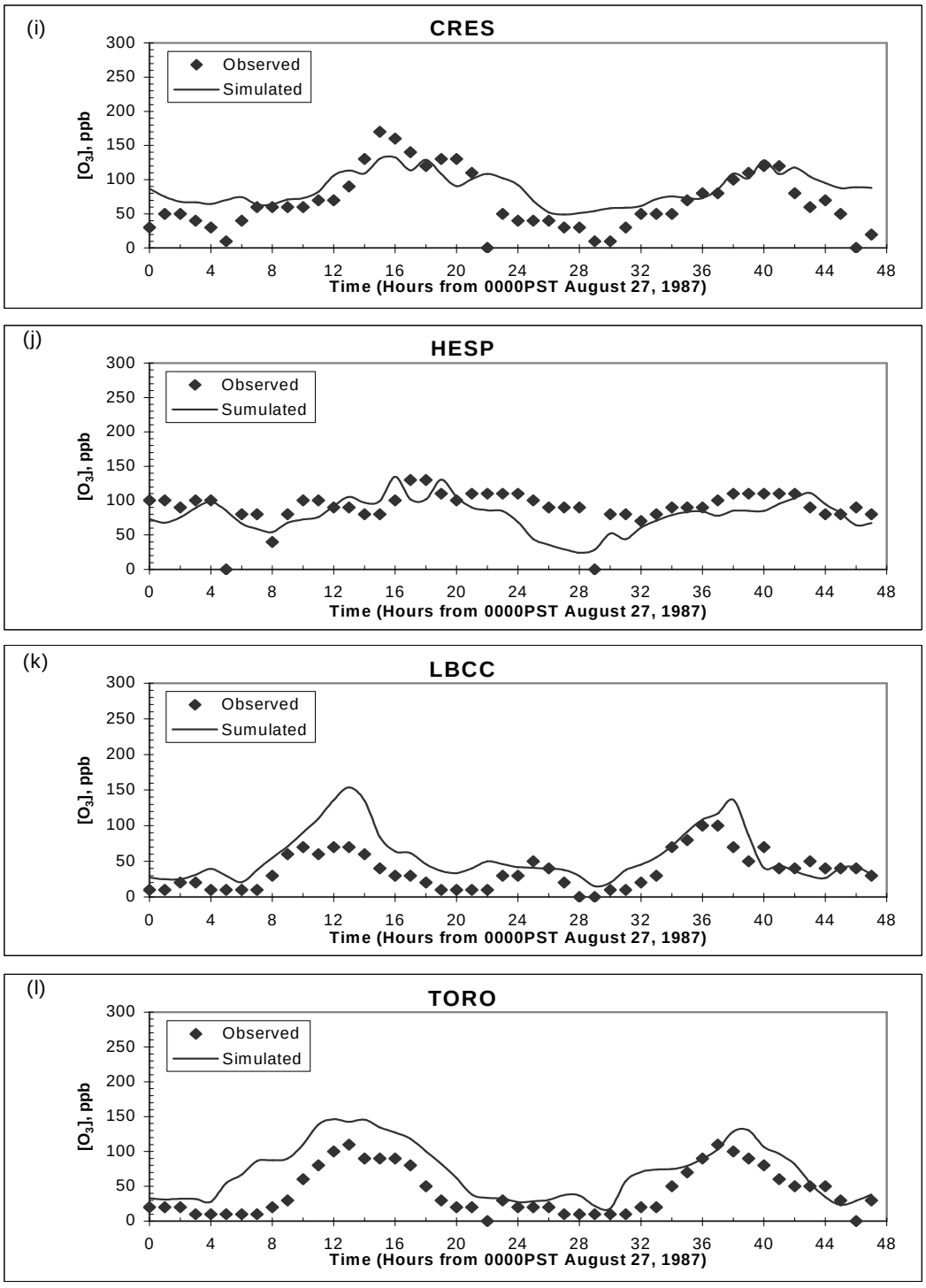

Figure 2 [con't]

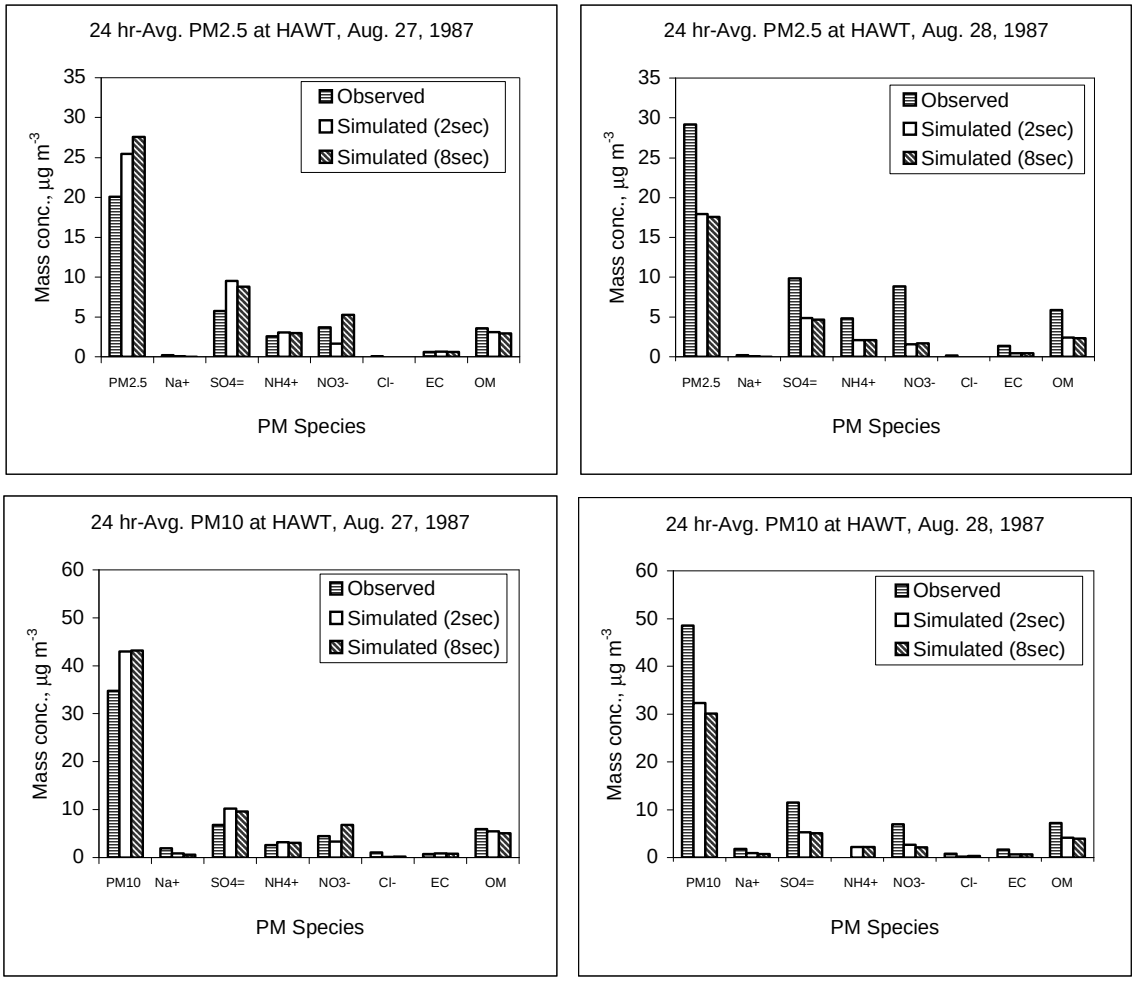

Figure 3. Observed and predicted 24-hr average concentrations for $PM_{2.5}$, PM_{10} and their chemical compositions on August 27-28, 1987 at Hawthorne [HAWT], CA.

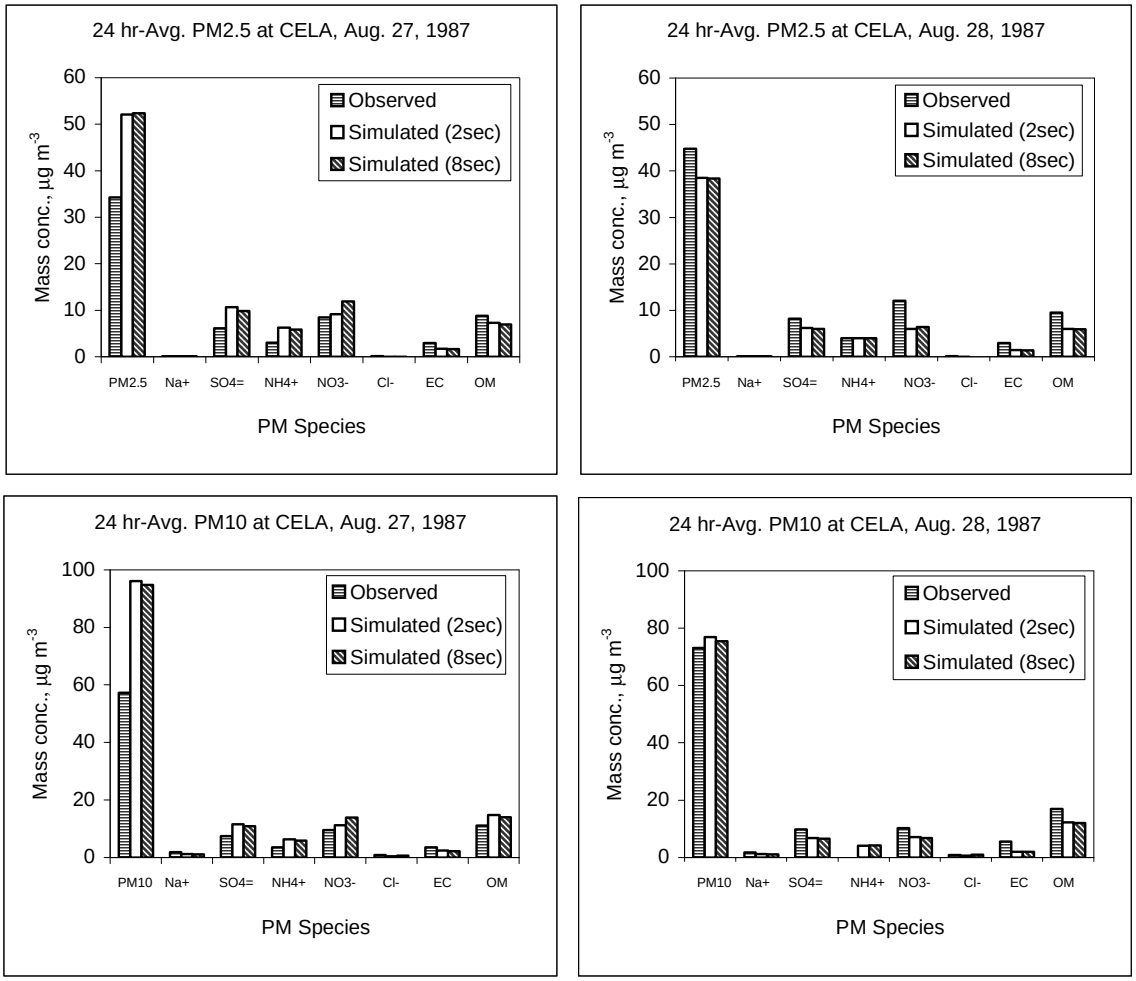

Figure 4. Observed and predicted 24-hr average concentrations for $PM_{2.5}$, PM_{10} and their chemical compositions on August 27-28, 1987 at Central Los Angeles (CELA), CA.

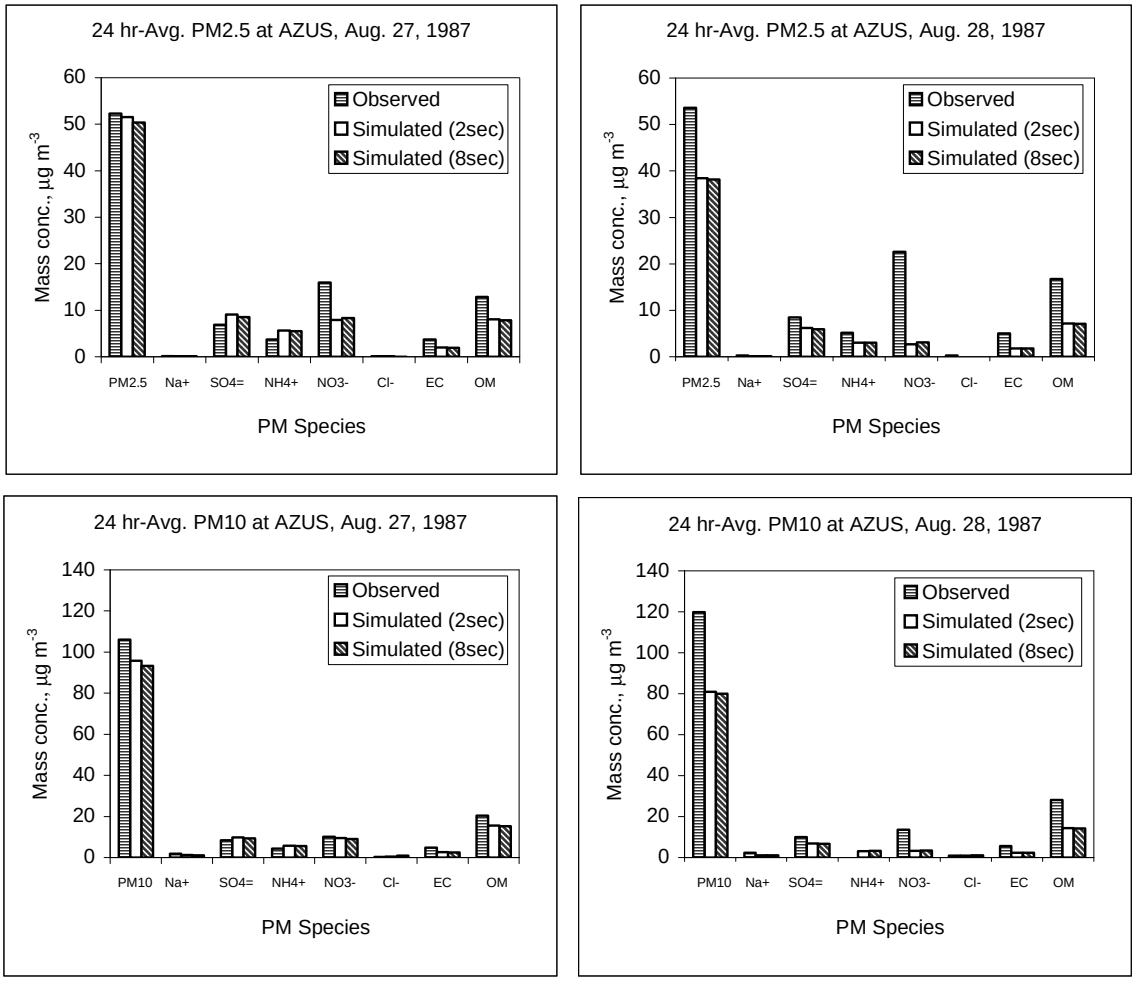

Figure 5. Observed and predicted 24-hr average concentrations for $PM_{2.5}$, PM_{10} and their chemical compositions on August 27-28, 1987 at Azusa (AZUS), CA.

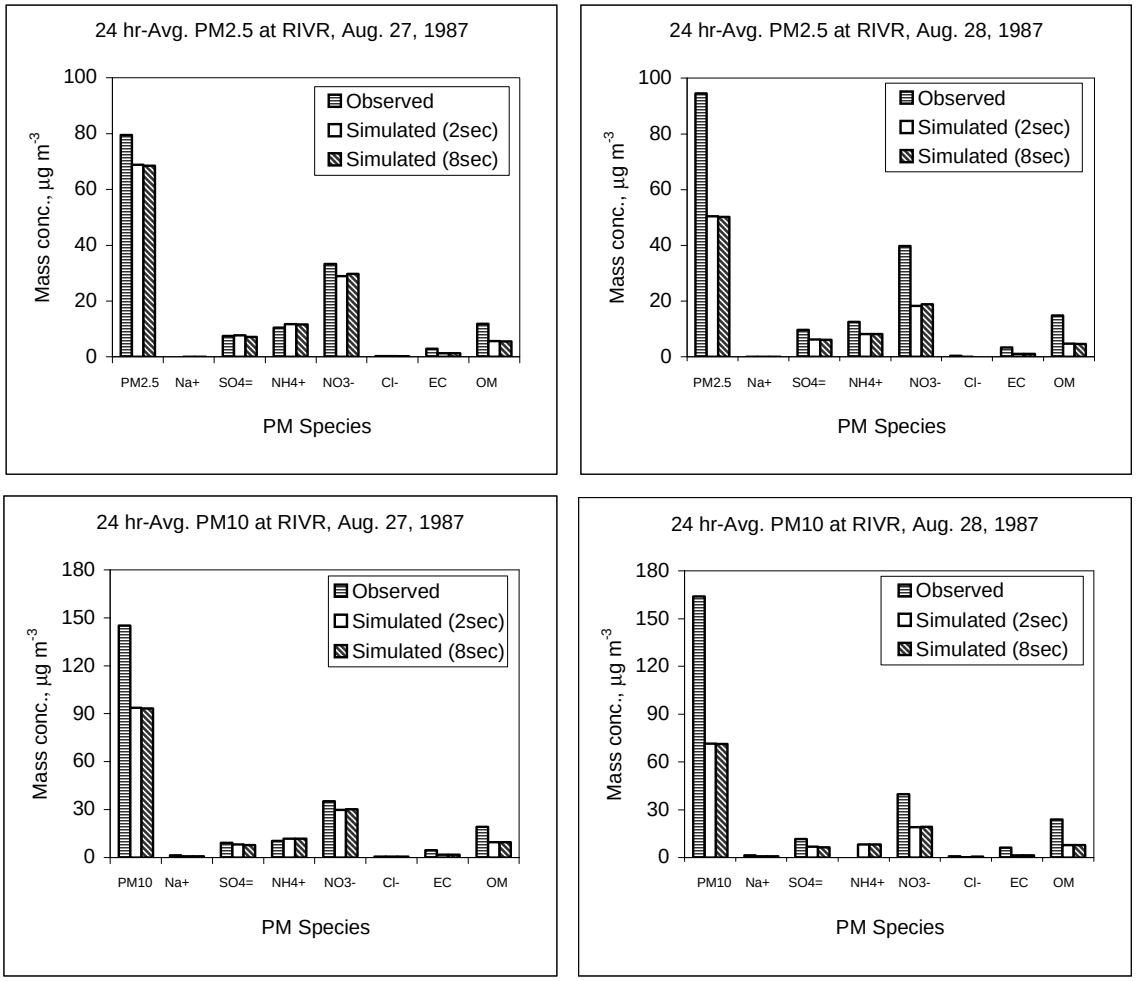

Figure 6. Observed and predicted 24-hr average concentrations for $PM_{2.5}$, PM_{10} and their chemical compositions on August 27-28, 1987 at Riverside (RIVR), CA.

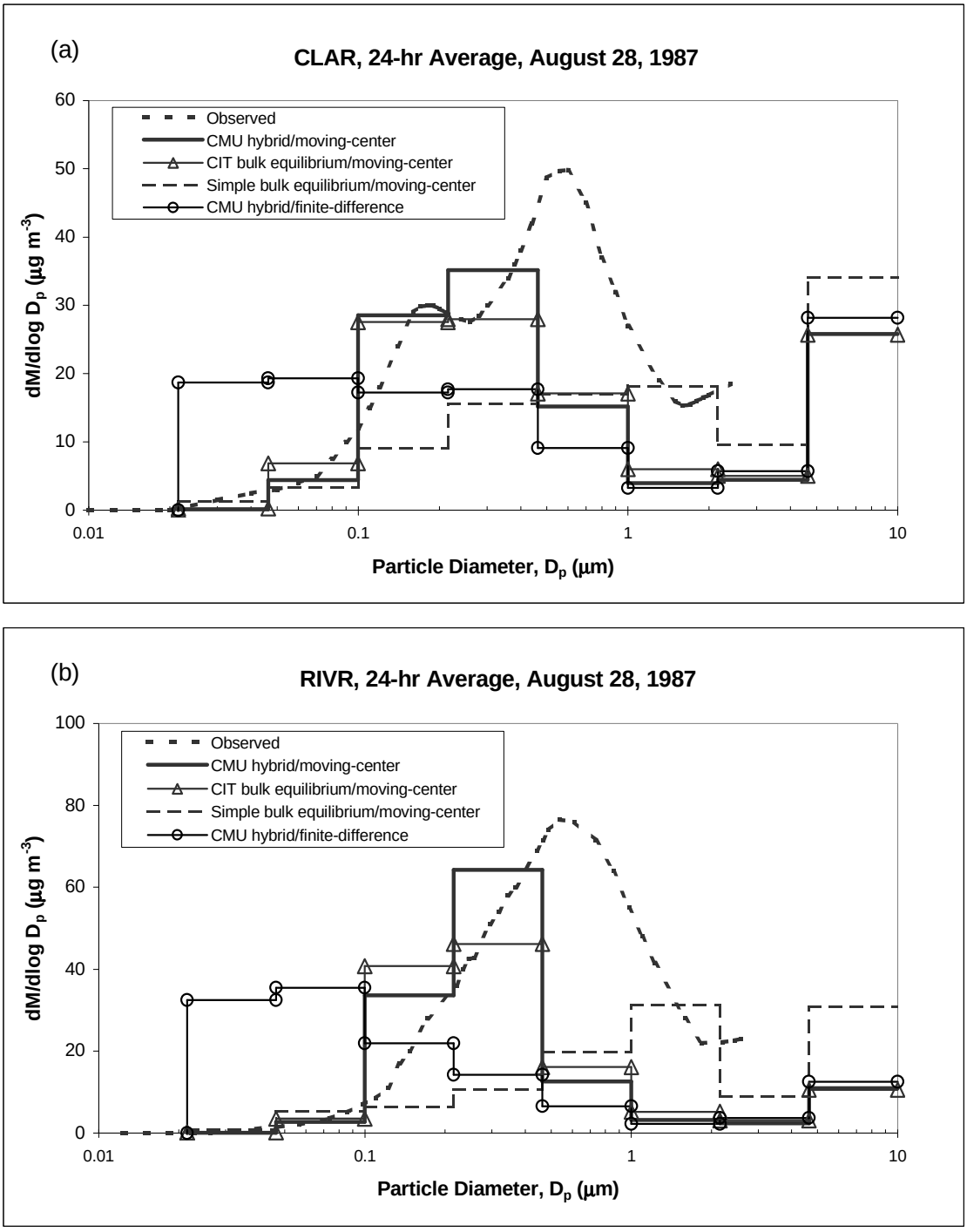

Figure 7. Observed average particle size distribution during 1987 SCAQS summer sampling periods (taken from Hering et al. (1997)) and predicted size distribution of 24-hr average $PM_{2.5}$ concentrations on August 28, 1987 at (a) Claremont (CLAR) and (b) Riverside (RIVR) with various combinations of condensational growth algorithm and gas/particle mass transfer approach.

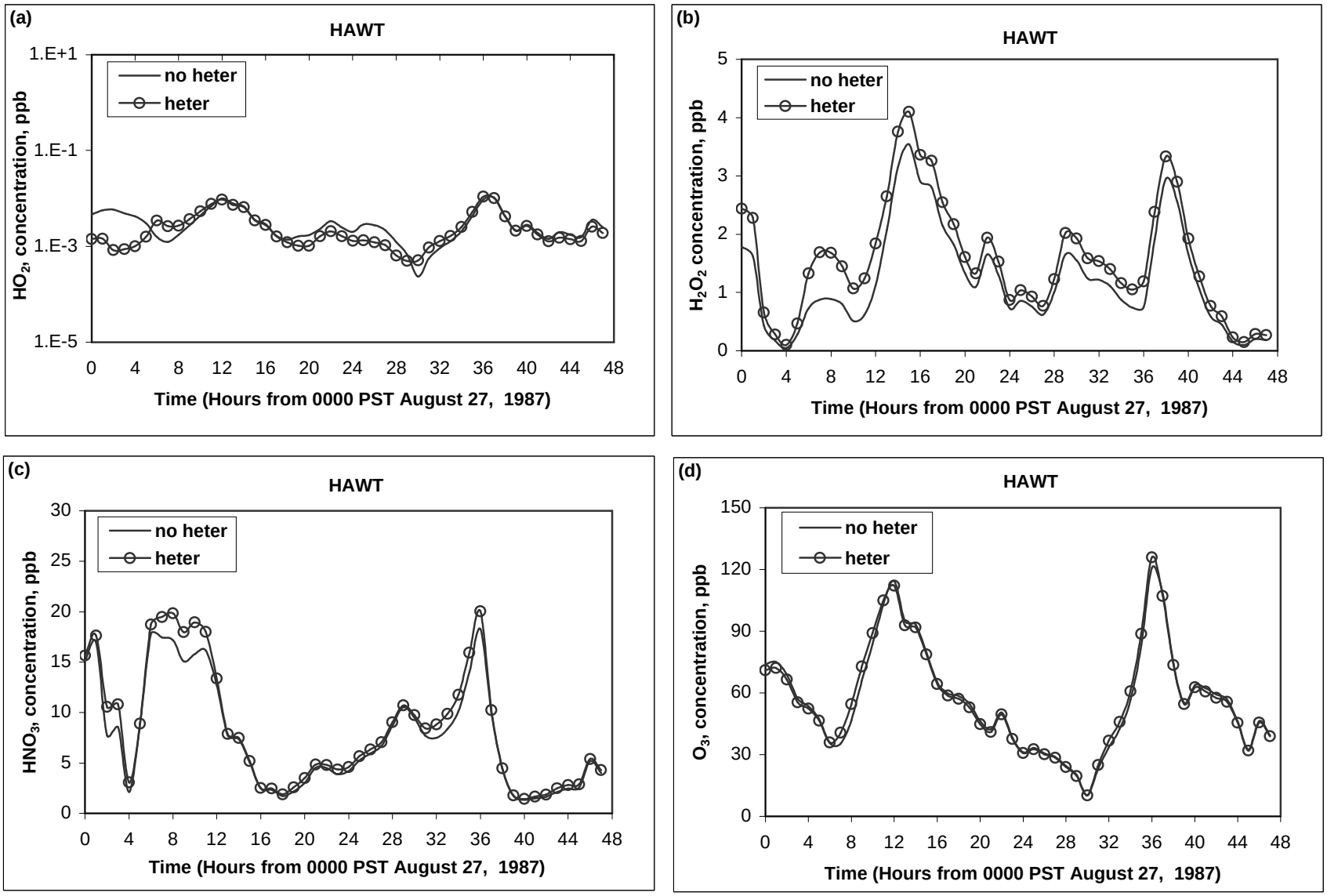

Figure 8. Predicted gas-phase mixing ratios of (a) HO_2, (b) H_2O_2, (c) HNO_3 and (d) O_3 at Hawthorne (HAWT) on August 27-28, 1987 with and without heterogeneous reactions. .

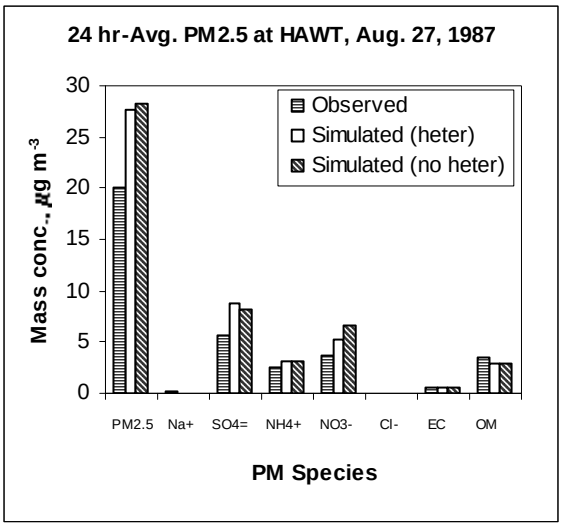

Figure 9. Observed and predicted (with and without heterogeneous reactions) 24-hr average mass concentrations of $PM_{2.5}$ and its chemical compositions at Hawthorne (HAWT) on August 27, 1987.

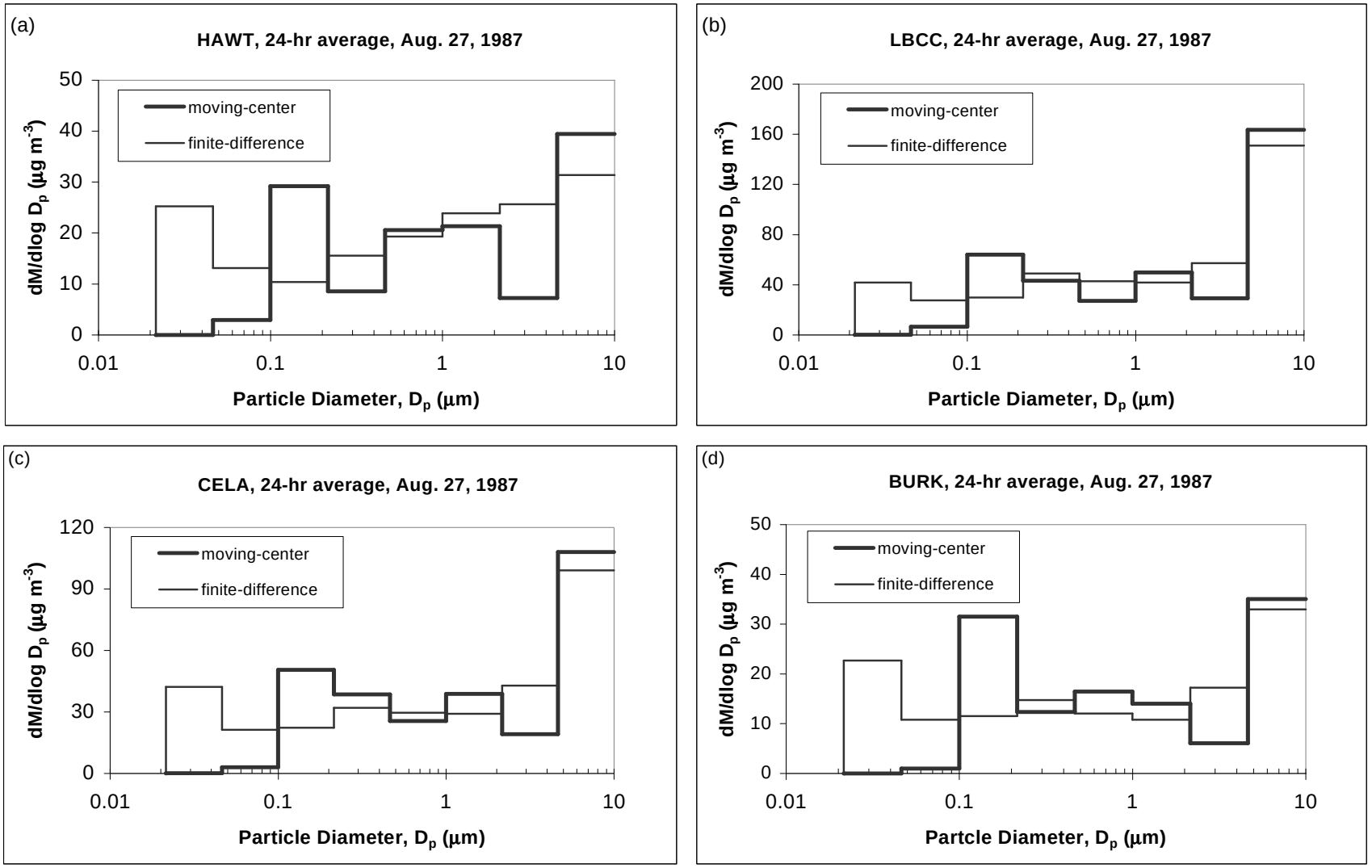

Figure 10. The particle size distribution predicted by the moving-center and the finite-difference schemes at (a) Hawthorne (HAWT), (b) Long Beach (LBCC), (c) Central Los Angeles (CELA) and (d) Burbank (BURK) on August 27, 1987.

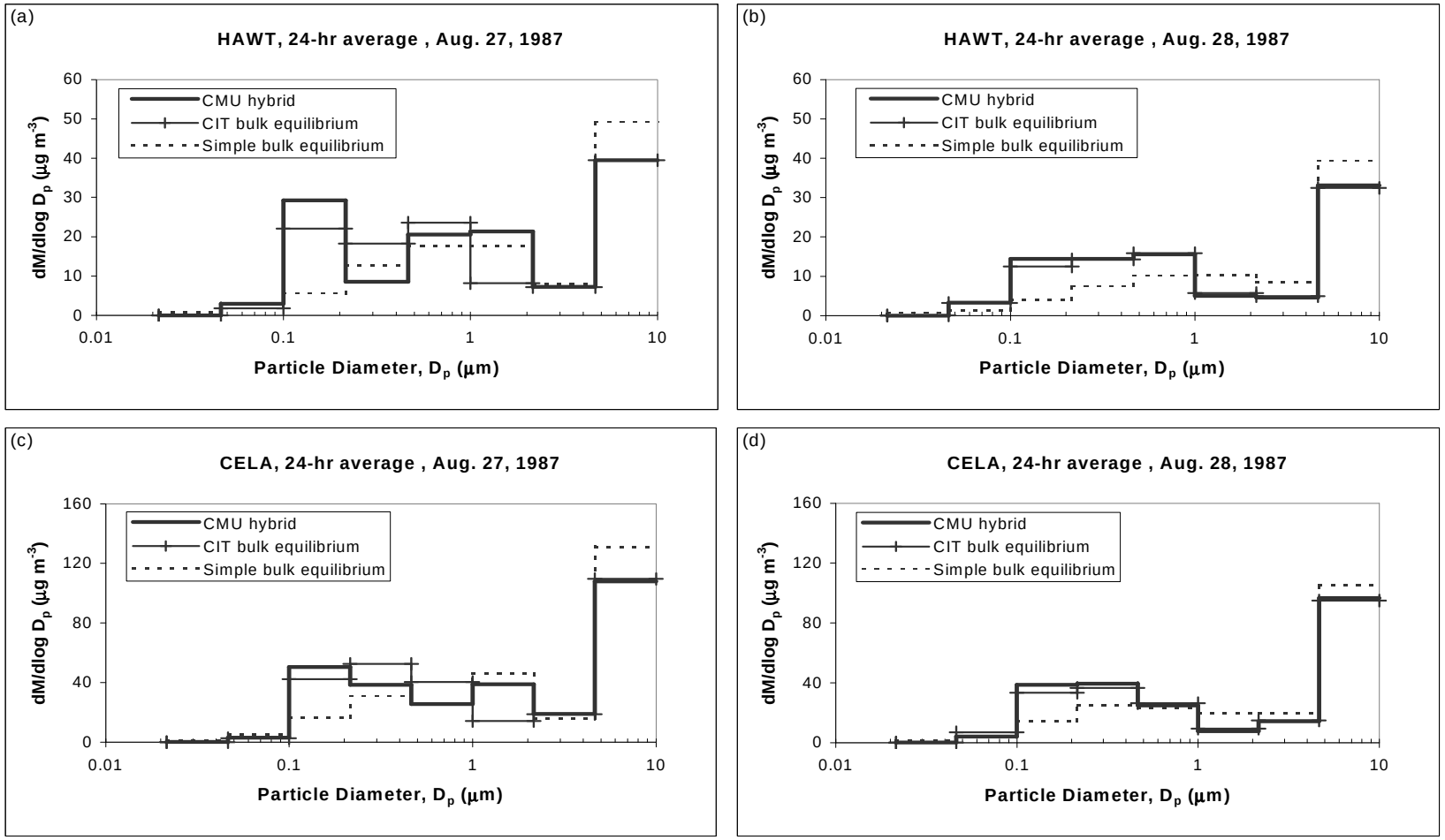

Figure 11. The total particle mass size distribution predicted with the CMU hybrid, the CIT bulk equilibrium and the simple bulk equilibrium approaches at Hawthorne (HAWT) ((a) and (b)) and Central Los Angeles (CELA) ((c) and (d)) on August 27-28, 1987.

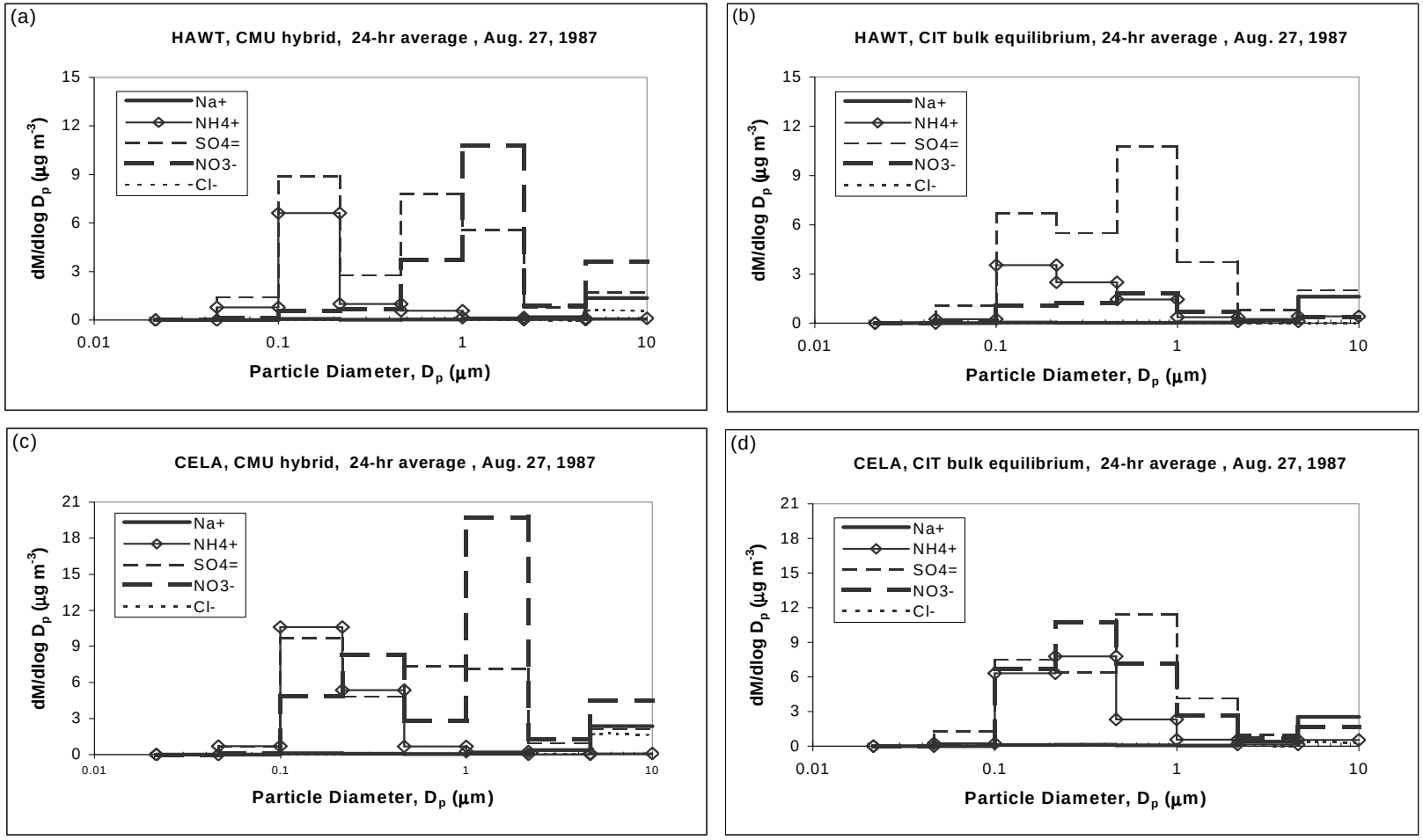

Figure 12. The mass size distributions of Na^+, NH_4^+, $SO_4^=$, NO_3^- and Cl^- predicted by the CMU hybrid and the CIT bulk equilibrium approaches at HAWT ((a) and (b)) and CELA ((c) and (d)) on August 27, 1987.